CHALMERS
UNIVERSITY OF TECHNOLOGY

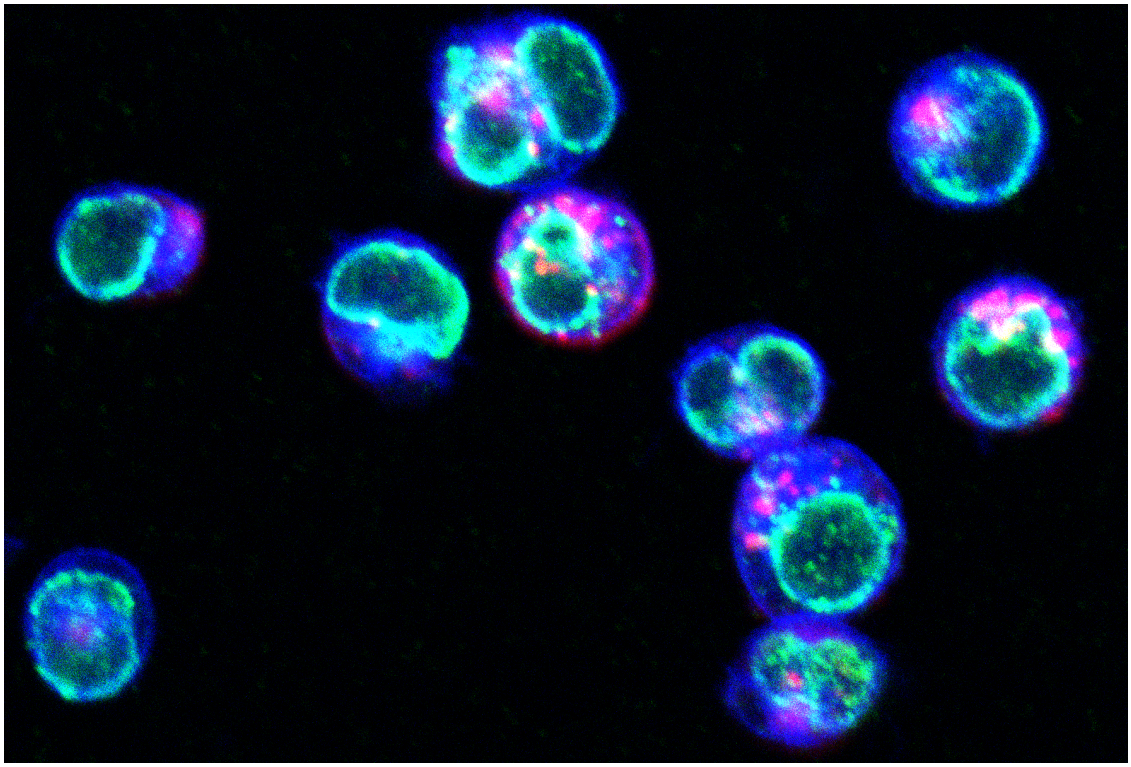

Cell Topography Correction in Colocalization Analysis

Improving Colocalization Analysis in Plasma Membrane by Normalization with Membrane Distribution

Master's Thesis in Biomedical Engineering

Sara Almehed

Department of Physics
CHALMERS UNIVERSITY OF TECHNOLOGY
Gothenburg, Sweden 2022

Master's thesis 2022

Cell Topography Correction in Colocalization Analysis

Improving Colocalization Analysis in Plasma Membrane by Normalization with Membrane Distribution

Sara Almehed

Department of Physics
Chalmers University of Technology
Gothenburg, Sweden 2022

Cell Topography Correction in Colocalization Analysis
Improving Colocalization Analysis in Plasma Membrane by Normalization with Membrane Distribution
Sara Almehed

Supervisor: Ingela Parmryd, Division of Medical Biochemistry and Cell biology, Department of Biomedicine, University of Gothenburg
Examiner: Fredrik Höök, Department of Physics, Chalmers University of Technology

Master's Thesis 2022
Department of Physics
Chalmers University of Technology
SE-412 96 Gothenburg
Telephone +46 31 772 1000

Cover: A cell image stack viewed as an RGB image with each channel corresponding to a fluorescent signal.

Typeset in LaTeX
Gothenburg, Sweden 2022

Cell Topography Correction in Colocalization Analysis
Sara Almehed
Department of Physics
Chalmers University of Technology

Abstract

Colocalization analysis is the study of the distributions of species with fluorescence microscopy. By estimating the spatial distribution of the fluoresence emission from two types of molecules, colocalization analysis is used as a method to help in the understanding of processes and interactions between molecules both within cells and with their environment. One of the basic assumptions of colocalization analysis today is that the species of interest are spatially distributed on a uniform surface, their only interaction being with each other. The assumption of a uniform surface however, does not always hold. The plasma membrane for example, is not flat but can be convoluted, folded and deformed in a large number of ways, causing the assumption of a flat surface to not be applicable when studying molecules present in the membrane of a cell.

With aim to improve the result of colocalization analysis, we present a method of intensity normalization by weighting the observed intensities of the species of interest by the membrane distribution. To study the effect of background normalization on colocalization analysis, simulations were conducted on non-uniform surfaces where the Pearson correlation coefficient and Spearman rank correlation coefficient were used to estimate the amount of colocalization before and after background normalization.

Based on the simulations, together with results from analysis of experimental images using confocal laser scanning microscopy, we present a proof of concept for the effect of background normalization on colocalization analysis.

Keywords: Colocalization analysis, T-cell, correlation, confocal laser scanning microscopy, Gaussian process regression, point processes

Acknowledgements

I have immensely enjoyed working on this project, through all ups and downs, covid-19 infections and experimental setbacks. Most of all I have learned a lot and would like to express my thanks. Thank you to my supervisor Ingela Parmryd. I also want to thank Ainsley Huang, who showed me around the lab my first weeks, without whom I probably still wouldn't know how to use a micro pipette. Thank you also to Jeremy Adler, who introduced me to ImageJ and spent hours in front of the microscope when I was unable to. Finally, I want to thank Victor Wåhlstrand Skärström, my greatest support, for always believing in me and my abilities.

Sara Almehed, Gothenburg, June 2022

Contents

List of Figures

1 Introduction

In biology, the interaction between molecules in cells carries great importance for their function. For example, the expression of receptors of the T-cell, a type of cell which is part of the human immune system, involves the interaction of several molecules. One such molecule is the protein CD59 which can be found gathered in membrane domains called lipid rafts, together with the T-cell receptors responsible for interaction with antigens [1, 2]. CD59 is a common surface protein found in many cell types, and its interaction with T-cell receptors was not obvious. However, as they were found to collocate in the same lipid rafts, their interaction was studied further and reviled a crucial role of CD59 in T-cell signalling [2]. In order to understand these important interactions the method of colocalization analysis has been developed, a method based on measuring the relationship between two molecules. In general, molecules in a cell is about five nanometers in size, making them too small to view independently in a common wide field microscope. By labeling the molecules of interest with a fluorophore, a chemical compound which emits light upon excitation, the emitted fluorescent light can be recorded using fluorescence microscopy, resulting in an image where the fluorescence intensity in a specific area is proportional to the amount of specie. In colocalization analysis the fluorescence signal of two or more species are compared either by studying their overlap, their correlation or by means of other mathematical measures of relation.

Fluorescence microscopy techniques such as single particle tracking or fluorescence recovery after photobleaching, both of which are used to study diffusion, assume a locally flat surface or membrane in order to estimate the diffusion coefficient of the particle of interest. This is an assumption which has carried over into the domain of colocalization analysis. However, the plasma membrane is not flat but can be convoluted, folded and deformed in a large number of ways, causing the assumption of a flat surface to not be applicable when studying molecules present in the membrane of a cell. For example, it has been proposed that the receptors of the T-cell, are located at the very end of long protrusions of the plasma membrane, in order to facilitate binding events [3]. Thus, it is insufficient to perform colocalization studies of species in these receptors without compensating for the membrane topography.

1.1 Purpose

Although it is often assumed, the plasma membrane of a cell is not flat, but can be folded and curved [4]. This topography affect the spatial distribution of the surface proteins, giving rise to a correlation between two molecules of interest, because of their mere presence on the plasma membrane. Adding a third fluorescent label which marks the membrane, the intensity distribution of this third label will correspond to the amount of membrane present in each pixel. By weighting the observations of the molecules of interest by this distribution, the impact of the topography on the colocalization analysis can potentially be mitigated.

The aim of this thesis is to attempt to correct the colocalization of molecules presented on the plasma membrane by taking intensity variation of the plasma membrane into account, and by doing so minimize the amount of false positive colocalization results.

1.2 Scope and Outline

This project is divided in theoretical simulations and experimental work and thus limited in its scope due to time and depth of analysis. The simulations are conducted in two dimensions, partly due to problem complexity, but also because colocalization analysis is most often conducted on 2D microscopy images on a 2D or 1D region of interest. The experimental work is restricted to colocalization in the plasma membrane of Jurkat T-cells and the method of analysis is limited by the resolution of a common confocal microscope with four excitation wavelengths. Furthermore, the experimental work is restricted by the available materials in the lab at the time of the project, severely limiting fluorophore combinations appropriate for combining three fluorescent labels.

Some fundamental concepts relevant for the project is presented in chapter 2. In order to give a brief overview of the biology of the experiments, the basic structure and key elements in the plasma membrane such as lipids and lipid phases are presented in this chapter. Some optical principles in microscopy such as point spread functions and aberrations relevant for the imaging with confocal microscopy are also presented. The chapter gives a short introduction to Gaussian processes which are used for both simulations and analysis. Finally, a more in-depth introduction to colocalization analysis is given which presents some common methods and the experimental outline of a colocalization study. Chapter 3 describes the experimental methodology used for cell culture, fluorescence staining and image acquisition. This chapter also describes the image processing and analysis conducted for the colocalization analysis and background normalization. Lastly, chapter 3 present the methods used for simulations, including a brief introduction to point processes. The results of the image analysis and simulations are presented and discussed in Chapter 4. Finally, the conclusions are presented in Chapter 5.

2 Background

2.1 The Cell Membrane

The cell membrane, or plasma membrane, is the outermost protective barrier of the cell which separates the inside of the cell from the outside environment [5]. The membrane is constructed as a lipid bilayer consisting of mainly phospholipids and cholesterol, visualizes in figure 2.1. Lipids have a hydrophilic, or polar, head and a hydrophobic fatty acid tail, which causes the lipids to order themselves in to a bilayer, with the tails protected against each other and the heads facing outward toward the water based environment. Apart from phospholipids and cholesterol the plasma membrane also includes the lipids sphingomyelin and glycolipids, as well as a wide variety of proteins with functions ranging from transportation of molecules through the membrane to signalling [5].

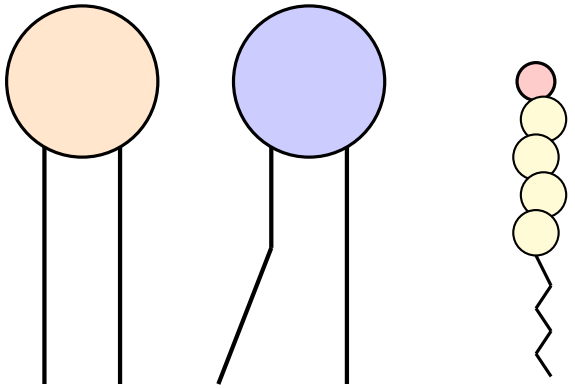

Figure 2.1: *Model of three types of lipids in the cell membrane. From left to right: Lipid with saturated fatty acid tails, lipid with an unsaturated fatty acid, cholesterol with hydroxyl head group (red) and carbon rings (yellow).*

The composition of the plasma membrane determines its properties, for example membrane fluidity. Rather than a solid, the plasma membrane is a viscous two dimensional fluid, meaning the lipids and membrane proteins are free to rotate and diffuse in the membrane [5]. Membrane fluidity is dependent on temperature and lipid composition, as lipids with shorter fatty acid chains interact weaker with each other than those with longer chains, thus allowing the membrane to have higher fluidity at lower temperatures. Lipids with unsaturated fatty acid chains also contribute to higher membrane fluidity as the double bond creates a kink in one of the chains, decreasing the lipids ability to pack together tightly [5]. Further, cholesterol have a small hydroxyl head group which inserts into the bilayer by the hydrophilic phospholipid heads, and four hydrocarbon rings which are rigid. Thus, inserting cholesterol into the membrane will lower its fluidity, due to the rigid hydrocarbon rings close to the phospholipid head groups, but since the cholesterol hinder interaction between fatty acid tails, it also acts to maintain fluidity at low temperatures [5].

The fluidity of the plasma membrane is an integral property for the functionality of the cell [5]. For example, it is believed that activated T-cell receptors present in ordered

microdomains in the cell membrane called *lipid rafts*, made up of sphingolipids, glycolipids and cholesterol [5, 6, 7]. Lipid rafts are realizations of what is called a *liquid ordered* membrane phase, because of the tight and ordered packing of lipids, as opposed to the *liquid disordered* phase of the bulk of the membrane [3]. The two lipid phases are illustrated in figure 2.2.

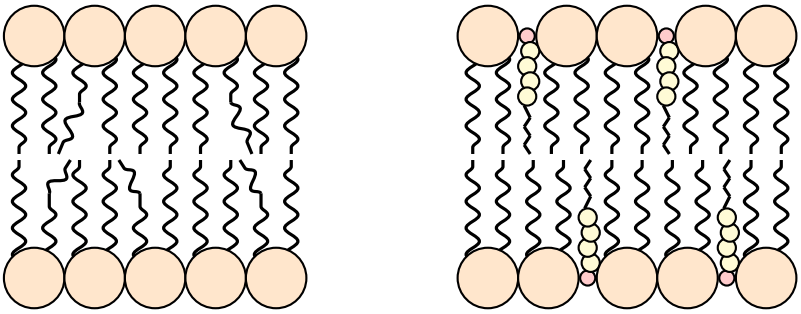

Liquid disordered *Liquid ordered*

Figure 2.2: *Model of membrane in liquid disordered phase (left) with both saturated and unsaturated fatty acid tails, and liquid ordered phase (right) where cholesterol is inserted in the membrane.*

As mentioned, there is an abundance of proteins inserted and attached to the plasma membrane, making up approximately half of the total mass of the plasma membrane [5]. A common model to describe the plasma membrane is the so called *fluid mosaic model*, where proteins inserted into the lipid bilayer are free to diffuse laterally in the membrane. However, the mosaic model has been revised as some proteins appears to be anchored to the cytoskeleton [5, 7], a network of protein filaments tasked with supporting the cell to be resistant to outward force and maintain its shape. Studies also suggest a correlation between liquid ordered domains and actin filaments of the cytoskeleton, implying a larger connection between the formation of lipid rafts and the cytoskeleton than that of lipid interactions [3]. Because of this, it is reasonable to assume that proteins found in lipid rafts are not there by accident, but prefer such membrane domains.

2.2 Optical Properties in Microscopy

Light microscopy is limited by some basic optical properties emerging from the nature of light. The light from the sample is gathered by the objective lens of the microscope into an image. In microscopy this property is often described by the *numerical aperture* (NA) $NA = n \sin\theta$, where n is the refractory index of the medium surrounding the lens and θ is the maximum half angle of the incident light cone. The numerical aperture of the lens directly influence the resolution of the microscope through the *Rayleigh criterion*. As light pass through the numerical aperture of the lens it diffracts according to *Huygens theorem*, creating a circular pattern called an *airy disc* visualized in figure 2.3, through interference with itself. The Rayleigh criterion then describe the resolution for the microscope, defined as the smallest distance between two points when the center of the airy disc of one point coincides with the first minimum of the second. For a microscope with numerical aperture NA_o for the objective lens and NA_c for the condenser lens, the Rayleigh criterion for light with wavelength λ can be described as

$$R = \frac{1.22\lambda}{NA_o + NA_c} =_{\{NA_o = NA_c = NA\}} \frac{0.61\lambda}{NA} \approx \frac{\lambda}{2NA}. \tag{2.1}$$

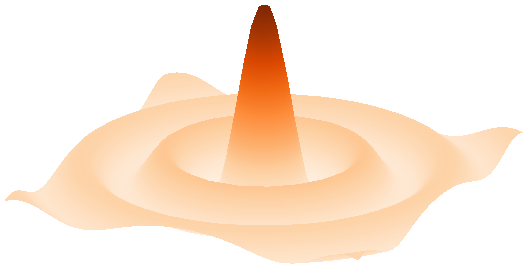

Figure 2.3: *3D representation of an airy function.*

The airy disc is often estimated by a *point spread function* (PSF), described as a Gaussian distribution approximating the center maximum of the airy disc. The PSF centered around (x_0, y_0) can then be described as

$$PSF(x, y) = \exp\left(-\frac{(x - x_0)^2 + (y - y_0)^2)}{2\sigma^2}\right), \tag{2.2}$$

where σ is the variance of the Gaussian, which is described by the full width half maximum (FWHM), i.e. the width of the PSF at half maximum intensity, and $FWHM = 2\sqrt{2\log(2)}\sigma$. When imaging, the lens convovles the image with the PSF. The 2D convolution of the image and PSF is defined as

$$J(x, y) = \sum_{i=-a}^{a} \sum_{j=-b}^{b} h(i, j) I(x - i, y - j), \tag{2.3}$$

where J is the convolved image, I the original image and h a kernel. In this case, h is the kernel corresponding to eq. 2.2, and the convolution results in a blurred image. In confocal microscopy, a pinhole the size of one airy unit is used to effectively exclude out of focus light in the acquisition, thus increasing the resolution with up to 30% [8].

The principles above are correct for a perfect lens, which are uncommon in practice. Imperfections can cause a wide variety of aberrations when imaging, such as *spherical* and *chromatic* aberrations which are illustrated in figure 2.4. Spherical aberrations arise when the rays close to the edge of the lens are refracted more than those close to the paraxial line, the center line through the lens. This causes the rays at the edge of the lens to converge before or after the focal point, which in turn produce an image which is blurry (out of focus) at the edges. Chromatic aberration is based on the principle that different wavelengths are refracted differently. There are two types of chromatic aberration, transverse and axial, where the principle of the last is quite similar to that of spherical aberration. Axial chromatic aberration arise when short wavelengths are refracted more than long wavelengths, resulting in the colours mixing, thus blurring the colors of the image. Transverse chromatic aberration occurs when the lens' magnification varies with wavelength, causing different wavelengths to focus on different points in the focal plane. Thus, when imaging using several fluorophores of different emission wavelength as in colocalization analysis, these aberrations may cause unwanted artefacts such as displacement of the channels or one channel being out of focus compared to another.

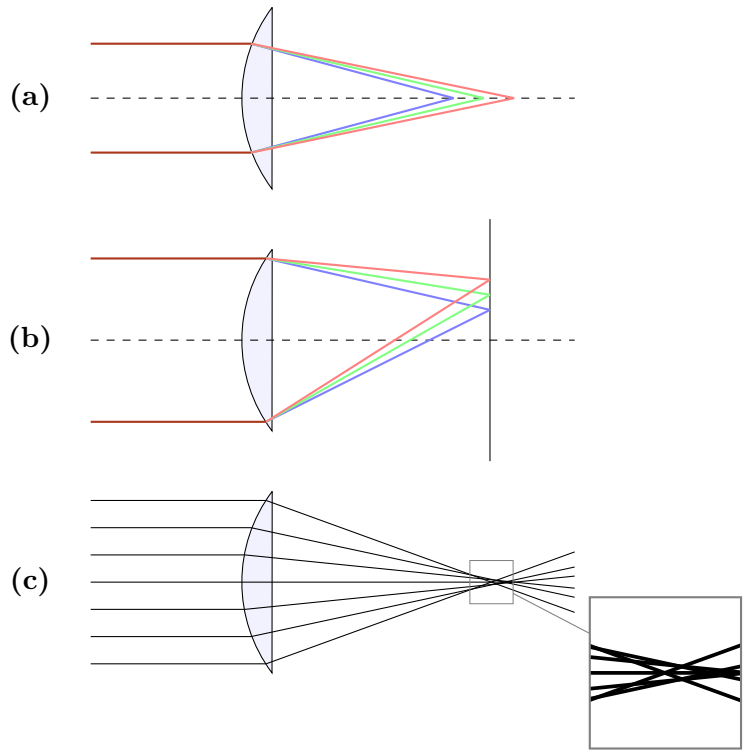

Figure 2.4: *Schematic illustration of three types of aberration of a circular lens. Axial chromatic aberration (a) where different wavelengths have different focal depth. Transverse chromatic aberration (b) where different wavelength are focused on different points in the focal plane. Spherical aberration (c) where the rays close to the edge of the lens are refracted more than those close to the paraxial line causing them to converge before the focal point.*

2.3 Gaussian Processes

A Gaussian process is a stochastic model, where each finite set of a signal is said to be described by a multivariate normal distribution, that is if for signal $\{X_t, t \in S\}$, the set $\{X_{t_1}, ..., X_{t_k}\}$ is a multivariate Gaussian, then $\{X_t, t \in T\}$ is a Gaussian [9]. These processes are widely used in both time series and geostatistical applications. In the latter application, the Gaussian process is represented as a random field in two dimensions with spatial dependencies instead of temporal [9].

A random field is a function $f(s)$, where the value at each point $s \in \mathbf{R}^n$ takes the value of a random variable. In two dimensions ($s \in \mathbf{R}^2$), the field may be visualised as an image, where the value of each pixel is a random variable. In the Gaussian random field, each pixel value belong to a multivariate Gaussian distribution, where the relation of each pixel and its neighbours are controlled by a covariance. Like a normal distribution is defined by its mean value and covariance matrix, a Gaussian process is completely characterized by it's mean $\mu_s = \mathbf{E}[X_s]$, where $\mathbf{E}$ is the expectation, and covariance function $C(s,t) = \mathbf{E}[(X_s - \mu_s)(X_t - \mu_t)]$ [9].

Fitting a Guassian process to a signal is called *Gaussian process regression* (GPR), or *Kriging* in spatial applications. GPR is a method of interpolation, and the idea is similar to linear regression, but instead of optimizing a linear function GPR optimises a multivariate Gaussian process to best fit the data. This method may be used as a way to predict values at unobserved locations in a model, which makes it useful for applications such as image

restoration of noisy, low quality images.

The basis of GPR lies in Bayesian statistics, where it is assumed that the observed data X belongs to an underlying, non-linear function $y(x)$, parameterized by β. Assuming some prior distribution $p(\beta)$ Bayes' theorem states

$$p(\beta|y, X) = \frac{p(y|\beta, X)p(\beta)}{p(y|X)}, \tag{2.4}$$

where $p(y|\beta, X)$ is the likelihood, $p(y|X)$ is the marginal likelihood and $p(\beta|y, X)$ is the posterior distribution. The GPR model take a Gaussian process prior

$$f(x) \sim \mathcal{N}(m(x), Q(x, t)), \tag{2.5}$$

where $m(x)$ is a mean function and $Q(x, t)$ a covariance function for the observed locations. From this, the values at unobserved locations can be estimated by combining the prior with the observed Gaussian likelihood function.

2.4 Colocalization Analysis

Colocalization analysis is the study of the distributions of two species (molecules, organelles, objects etc.) with fluorescence microscopy. It is used as a method to help in the understanding of processes and interactions between the species both within cells and with their environment, by estimating their interactions from their distributions [10, 11]. Colocalization analysis is generally divided in two subgroups, co-occurence and correlation [10]. Co-occurence studies whether two molecules are found in the same organelle, while correlation addresses whether there is a relationship between the spatial distributions of two molecules. Colocalization methods are typically divided in intensity-based and object-based methods.

2.4.1 Object-Based Methods

In object-based methods, each object (molecule, organelle, vesicle etc.) is represented by a single point. Most often the point spread function of the recorded fluorescent light is larger than the size of a single pixel, which means that the coordinates of each point must be estimated. This can be achieved by the use of wavelet-based methods and subsequent fitting of point spread functions [11, 12]. The resulting point patterns may then be modeled using marked point processes, a stochastic mechanism where the pattern is a realization of the distribution of the process. In a marked process each point, which is called *event* in a point process, is assigned a quantity. In the case of colocalization we have two marks representing the type of molecule. This process can be analyzed using second order statistics such as Ripley's K, or adaptions thereof [13].

Ripley's K produces a measure of the clustering in a point pattern by counting the number of events within a radius r of another specific event [14]. It is defined as

$$K(r) = \frac{1}{\lambda}\mathbf{E}[\#\text{further events within radius } r \text{ from a typical event}], \tag{2.6}$$

where λ is the intensity of the process, which can be estimated by the number of events

per unit area [14]. An unbiased estimate for Ripley's K is given by

$$\hat{K}(r) = \frac{1}{n\hat{\lambda}} \sum_{i=1}^{n} \sum_{i \neq j} w(x_i, x_j) 1(\|x_i - x_j\| < r), \tag{2.7}$$

where $w(x_i, x_j)$ is a boundary correction term, and $\hat{\lambda}$ is the estimated intensity.

Ripley's K-function can easily be adapted to marked point processes. For a process with marks A and B, with intensities λ_A and λ_B respectively, the $\lambda_B K_{AB}$ function produce a measure the amount of clustering of events with type A around events of type B, by giving the mean number of events of type A in a disc with radius r around an event of type B, see figure 2.5.

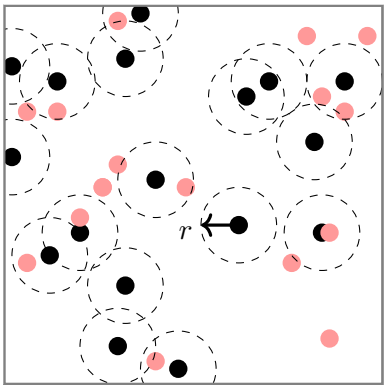

Figure 2.5: *Visualization of Ripley's K-function in a marked point process with two marks/species.*

Another common object-based method to investigate colocalization between two species in a marked point process is by the nearest neighbour distance function. This function is described by the probability of an event within a radius r of another event [11],

$$G(r) = P(D_1 \leq r), \tag{2.8}$$

where D_1 is the distance from an event to its nearest other event. For a spatial uniformly random pattern, this function is described as

$$G(r) = 1 - e^{-\lambda \pi r^2}, \tag{2.9}$$

and thus patterns with $G(r)$ higher than that of eq. (2.9) tends to be clustered. By calculating the nearest neighbour function of events of type B around events of type A, results of clustering can be an indication of colocalization.

The application of point processes in colocalization analysis demand a "spotty" image, where each object of interest is individually represented. This is often not the case, because of low resolution and the unknown amount of fluorophore in each intensity peak [11, 15]. In these cases intensity based methods, which focus on the intensity content of the image, can be preferred.

2.4.2 Intensity Based Methods

Intensity based methods use the intensity values of the pixels in an image, treating the images as signals without necessarily taking spatiality into account. By doing so, more general signal analysis methods can be used to evaluate the intensity information of an image, for example correlation measurements. Two species belonging to correlated populations can be indication of colocalization [11]. The correlation is measured by the calculation of correlation coefficients for the images, for colocalization analysis the most common correlation coefficient are the Pearson correlation coefficient and the Spearman rank correlation coefficient [10, 11]. In an image with two channels A and B, and the intensity information of pixel i is denoted I_A^i and I_B^i, the Pearson correlation coefficient is

$$\rho_{AB} = \frac{\text{cov}(I_A, I_B)}{\sigma_A \sigma_B} = \frac{\sum_i (I_A^i - \bar{I}_A)(I_B^i - \bar{I}_B)}{\sqrt{\sum_i (I_A^i - \bar{I}_A)^2 \sum_i (I_B^i - \bar{I}_B)^2}}, \tag{2.10}$$

where $\text{cov}(I_A, I_B)$ is the covariance and σ_A and σ_B are the standard deviation of each channel [16]. The Pearson coefficient is the coefficient of the linear fit, by simple linear regression, to the intensity scatter plot between the two channels as visualizd in figure 2.6. It measure the amount of intensity in channel A which can be explained by channel B and produce a value $\rho \in [-1, 1]$ where 1 is perfect correlation, 0 is no correlation and -1 is perfect anti-correlation [11].

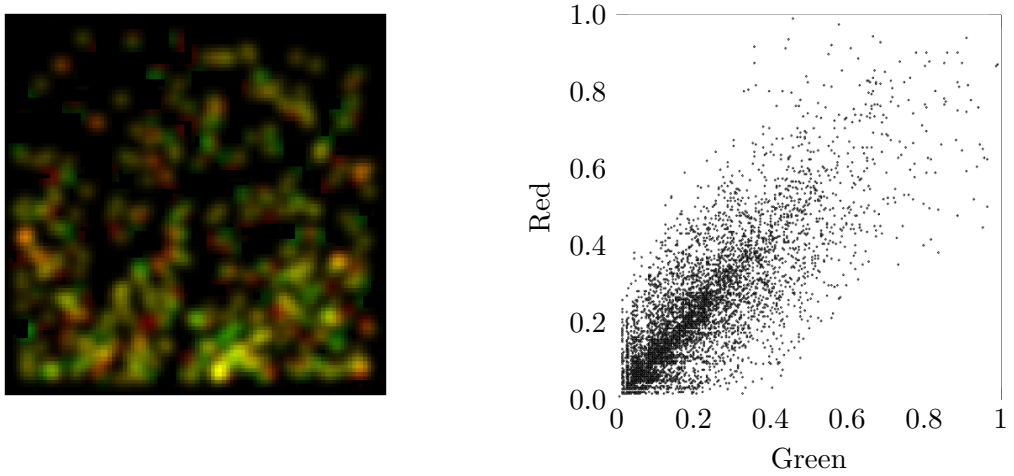

Figure 2.6: *(a) Simulation of a marked point process with two species (red and green). Each process has a samples size of $n = 1000$. (b) Intensity scatter plot of values in simulation in (a).*

A drawback with the Pearson correlation coefficient is that it is sensitive to outliers with high intensity values [17]. Moreover, the coefficient assume a linear correlation between signals, which is not always the case. An alternative, in order to lessen this impact, is by the use of the Spearman rank coefficient, in which the Pearson correlation coefficient is computed for the rank of the intensity values instead of the intensities themselves [17, 18]. Here, the rank is the order of intensity, where the pixel with lowest intensity will have the lowest rank, and the pixel with the highest intensity will have the highest rank. The

Spearman rank correlation coefficient is defined

$$\rho^s_{AB} = \frac{\text{cov}(R(I_A), R(I_B))}{\sigma_{R(I_A)}\sigma_{R(I_B)}}, \tag{2.11}$$

where $R(I_A)$ and $R(I_B))$ is the rank of the signal I_A and I_B respectively.

Another common measure for colocalization is the Mander's coefficient [19]. The Mander's coefficient is designed to take variation in intensity between channels into account. For a two channel system with intensities I_A and I_B the Mander's coefficients describe the amount of intensity in channel A which overlap with channel B, the coefficients can be written as

$$M_{A\cap B} = \frac{\sum_i I^i_{A\cap B}}{\sum_i I^i_A}, \tag{2.12}$$

$$M_{B\cap A} = \frac{\sum_i I^i_{B\cap A}}{\sum_i I^i_B}, \tag{2.13}$$

where $I^i_{A/B}$ is the intensities for each pixel i in channel A and B respectively and $I^i_{A\cap B} > 0$ if $I^i_B > 0$ and $I^i_{B\cap A} > 0$ if $I^i_A > 0$ [19]. It is worth pointing out that while the Pearson correlation coefficient $\rho_{AB} = \rho_{BA}$, M_A is not necessarily equal to M_B.

The motivation of the choice of method used for colocalization studies has been discussed at length. It has been argued that the Pearson correlation coefficient is to prefer over the Mander's coefficient, especially in images with low resolution and high particle density [15]. However, it has also been argued that while the choice between the Mander's coefficient and Pearsson correlation coefficient should be decided by the biological context of measurements, the Spearman rank coefficient should always be preferred above the Pearson correlation coefficient [18].

2.4.3 Experimental Outline

A colocalization experiment can be divided in two parts: Image acquisition and analysis. The first step of colocalization analysis is choosing a biologically relevant specimen, as false correlation can occur if two species are found in different, but accidentally overlapping organelles. The second is the choice of fluorophores. When measuring colocalization it is important that the emission and excitation spectra are distinctive, as overlapping spectra will result in so called cross-talk and bleed-through. Cross-talk arise when the emission spectra of two fluorophores overlap to such an extent that they will be excited by the same excitation laser, whereas bleed-through is the phenomena where overlap in emission spectra cause emission of a fluorophore in the wrong channel [8]. One such example is visualized in fiures 2.7a and 2.7b, where the two fluorophores DiI and Alexa Fluor-488 have significant overlapping excitation and emission spectra, causing cross-talk and bleed-through when excited by a laser of around 488 nm.

While selecting a good combination of fluorophores will minimize the risk of overlap, completely eliminating it is difficult, as many excitation and emission spectra have long tails. In order to maximize the emission while ensuring no cross-talk or bleed-through, filters are used when acquiring images. The ability to acquire images consecutively, i.e exciting and imaging one channel at a time is preferable to limit bleed-through [10]. Several imaging systems can be used for colocalization analysis, the only requirements being conse-

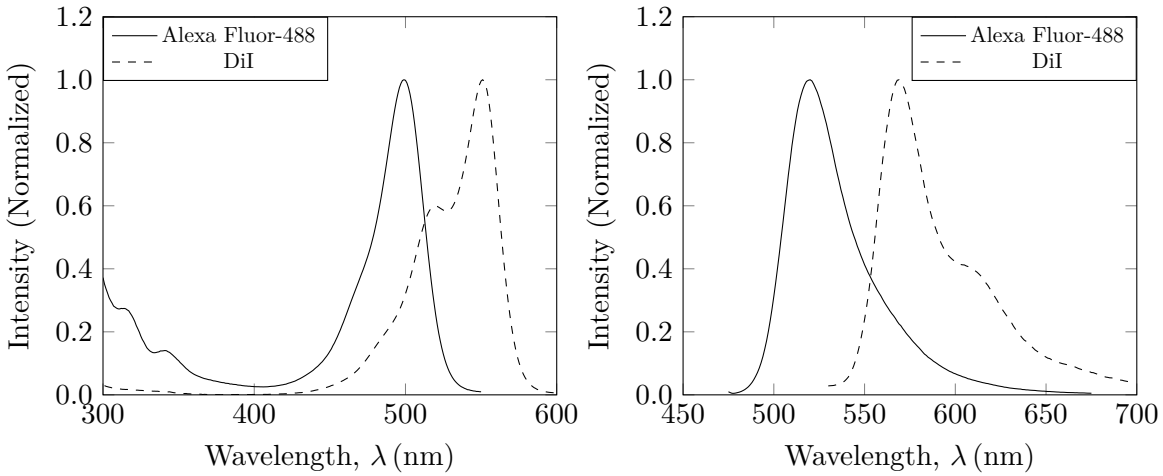

(a) *Excitation spectra for DiI and Alexa Fluor-488.*

(b) *Emission spectra for DiI and Alexa Fluor-488.*

Figure 2.7: *Demonstration of cross-talk and bleed-through for fluorophores DiI and Alexa Fluor-488. Because of their overlapping excitation spectra (a), DiI and Alexa Fluor-488 will both be excited by the same laser at wavelength* 488 nm *resulting in what is known as cross-talk. The overlapping emission spectra (b) will result in a bleed-through of Alexa Fluor-488 into when studying DiI and vice versa.*

quitive imaging in two channels, for example confocal microscopes, widefield microscopes, and total internal reflection microscopes [10].

As described in section 2.2, the image signals captured by a microscope is not a perfect representation of the sample. Moreover, the image may be distorted by some noise, making image processing important before performing colocalization analysis. Noise can originate from a number of sources, and processing will differ depending on the type of noise. Poisson noise, for example, originates from the random counting process from photonic light, is prominent in microscopes due to the use of photon counting detectors [20]. The arrival of a photon to the sensor is random and independent and can be described as a temporal Poisson process with distribution

$$P(N = n) = \frac{(\lambda t)^n}{n!} e^{\lambda t}, \tag{2.14}$$

where $N = n$ is the number of photons which has reached the sensor at time t and λ is a shape parameter. This gives the expected photon count and variance $\mathbf{E}[N] = \mathrm{Var}[N] = \lambda t$. Poisson noise originates from the uncertainty of this process and as the variance of the distribution is the same as the expected value, the noise is signal dependent with signal to noise ratio

$$\mathrm{SNR} = \frac{N}{\sqrt{N}}. \tag{2.15}$$

Because of this, noise is minimized when the signal is large, as even though the noise increase with signal strength, the signal to noise ratio will decrease. Some of the noise can be removed by taking several consecutive images in each channel and averaging [8, 20]. Another commonly occurring noise is background signal, arising from natural fluorescence or the sample preparation. In case of a uniform background signal, this effect can be removed by subtracting the mean value of the background from every pixel of the image.

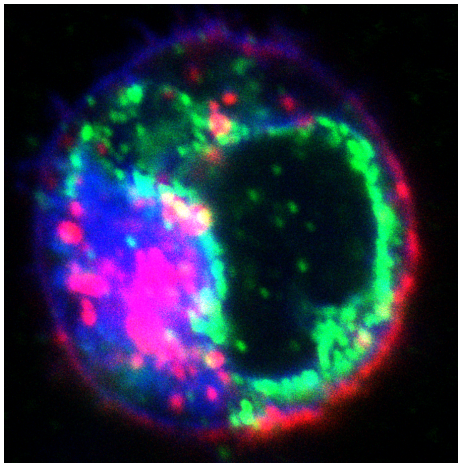

Figure 2.8: *A cell with three channels (red, green, blue). Both the red and the blue channel are present in the plasma membrane of the cell, but due to chromatic aberration the two channels are shifted and are not overlapping as one would expect.*

Other common sources of noise are electronic and thermal interference from the imaging system which may be minimized by keeping the electronics cool [8].

Furthermore, the channels must be corrected for misalignment of the channels, an effect which may arise from chromatic aberration. Microscopes today often correct for misalignment, but there is often a few artefacts left especially when it comes to fluorescence at opposite ends of the spectrum. This may be seen in figure 2.8 where the blue and red signals should both be present in the plasma membrane, but are spatially shifted with respect to each other, rather than overlapping. This can be solved by simply shifting the channels so they overlap, for example by means of image registration, a method of transforming images into the same coordinate system.

The colocalization analysis is typically conducted on a biological region of interest (ROI). The ROI can be the entire image or the part of the image where signal is expected to be found, for example a cell, the cytoplasm or the cell membrane. The ROI is generally picked by a segmentation method, often thresholding, manual segmentation or a combination of the two. Conducting the analysis in a ROI is important, as the background is most likely a large area which is of no interest to the analysis but none the less will influence the result. Although the background is zero everywhere, there is a large amount of pixels which coincide exactly between channels, causing a false correlation. In figure 2.9 some ROI's of a cell produced by global and adaptive thresholding, manual selection and a combination of global thresholding and manual selection are presented.

The degree of colocalization may be computed by means of either object-based or intensity-based methods, depending on the nature of the images. To increase the accuracy of the analysis one can perform replicate-based noise-corrected correlation (RBNCC) [17]. RBNCC is a method which uses two consecutively captured images and corrects the correlation coefficient based on the mean correlation coefficient between all channels. For example for two images with with a red (R) and a green (G) channel each R_1, R_2, G_1, G_2, with cross correlations ρ_{G_1,R_1}, ρ_{G_1,R_2}, ρ_{G_2,R_1}, ρ_{G_2,R_2} and auto correlations ρ_{G_1,G_2}, ρ_{R_1,R_2}, the corrected correlation is

$$\mathrm{P} = \frac{1}{4}\frac{\rho_{G_1,R_1} + \rho_{G_1,R_2} + \rho_{G_2,R_1} + \rho_{G_2,R_2}}{\sqrt{\rho_{G_1,G_2}\rho_{R_1,R_2}}}. \tag{2.16}$$

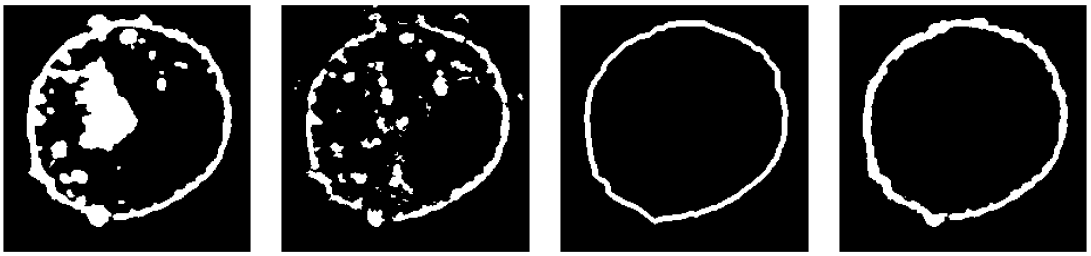

(a) *Global thresholding with threshold* $t = 0.05$.

(b) *Adaptive thresholding using the mean value of each pixel neighbourhood to estimate the threshold.*

(c) *Manual selection based on selecting the brightest pixels followed by dilation of 2 pixels.*

(d) *Combination of global thresholding with threshold* $t = 0.05$ *and manual selection followed by dilation of 5 pixels.*

Figure 2.9: *Some examples of ROI selection by segmentation using thresholding (a and b), manual selection of brightest pixels in the plasma membrane (c) and a combination of the two (d).*

Of course, two independent spatially distributed species are not colocalized. However, there will still be a degree of intensity overlap between the points resulting in a false correlation [21], and it is thus of interest to investigate the significance of estimated correlation coefficients. One such measure of significance, presented by Costes et al. [21], evaluates the correlation coefficient by comparing it to coefficients produced by two independent distributions by scrambling the observations in one channel and computing the correlation coefficient again. Repeating the process a large number of times ($n = 200$ in [21]) the significance of the original correlation can be estimated, as the resulting p-value is inversely correlated to the probability of getting a similar or more extreme correlation coefficient from a random signal [8]. Another method of measuring the significance of correlation in colocalization analysis is presented by Van Steensel et al. [22] where the cross-correlation function is estimated by calculating the correlation coefficient after shifting one channel a small distance δx with regards to the other. If the resulting correlation coefficients has their maximum at $\delta x = 0$ the correlation may be deemed significant.

3 Methods

3.1 Experimental Work

The experimental work constitutes a significant part of the project, the largest part of which consisted in developing and evaluating methods of staining and preparing samples. This process is time consuming and sensitive, and the procedure of which will be covered in this section.

3.1.1 Cell Culture

The cells used for the colocalization study were grown in a cell culture, a method of sustaining cells outside of their natural environment. 20 mL of cell culture consisting of Jurkat T-cells in suspension in RPMI-1640 medium with 1% antibiotics (Pen/Strep) to prevent infection, 10% Fetal Bovine Serum to resemble the environment of blood, and 2 mM L-Glutamine for nurishment, was held in a cell culture flask in an incubator at 37 °C, 5% CO2 and 90% humidity. For optimal growth conditions, the density of cells in the cell culture should be between $2 - 3 \cdot 10^5$ cells/mL and should not exceed $3 \cdot 10^6$ cells/mL. To maintain the cell density the cells were counted and medium replenished every 2-3 days.

The cell density was calculated by the counting of cells using a hemocytometer. 10 µL cell culture was mixed with 10 µL of Trypan Blue which stains dead cells blue, before administring 10 µL of stained cell culture on the hemocytometer. Using a microscope with 10 times magnification, the cells can be seen on a grid as in figure 3.1. Assuming each 4×4 corner square contains 0.1 µL fluid, the total cell density can be estimated by counting the non-colored cells in the corner squares and calculating

$$\#\text{cells} = \frac{N_1 + N_2 + N_3 + N_4}{4} \frac{p}{V_0}, \tag{3.1}$$

where N_i, $i = 1, 2, 3, 4$, is the number of cells in each corner square, p is the dilution with Trypan Blue and V_0 is the volume of each corner square. In this project $p = 2$ and $V_0 = 0.1\,\mu\text{L}$.

The cell culture is very sensitive to bacterial infection, and proper measures must be taken to prevent such infections. All materials in contact with the cell culture were sterile, and all work were performed on a sterile bench cleaned with 70% EtOH before and after use, and sterilized further with UV-light after use. Any materials brought into the lab was cleaned with 70% EtOH. Further, gloves, lab coat, clean slippers, and surgical mask were worn at all time when working with the cell culture.

3.1.2 Sample Preparation and Methodology Development

Before staining the cells for fluorescence microscopy, the cells from the cell culture were washed with serum free medium by centrifuging and re-suspended in phosphate-buffered saline (PBS) to $1.25 \cdot 10^6$ cells/mL. The washed cells were then attached to TESPA coated glass coverslips by placing 200 mL cellsuspension on the coverslip on ice. TESPA (3-aminopropyltriethoxysilane) a reagent which binds to glass through the silane, allowing

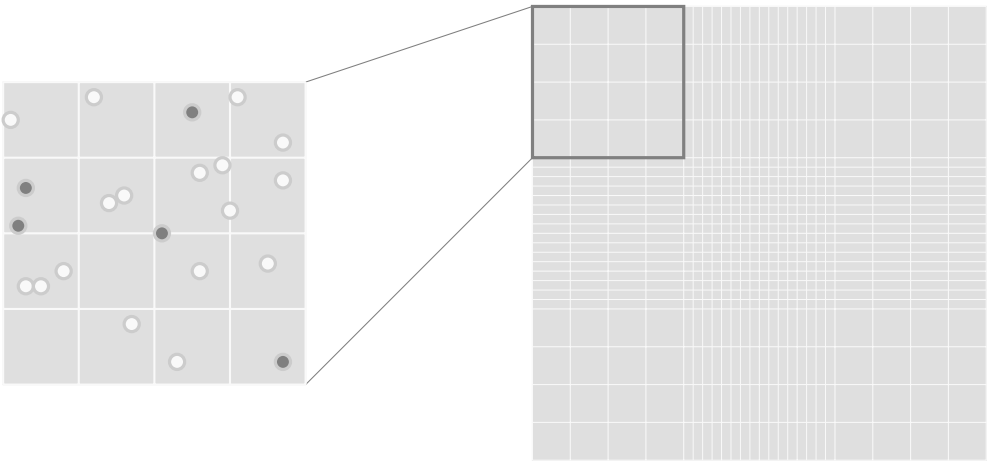

Figure 3.1: *Counting grid of a hemocytometer used for counting cells in a cell culture. The number of alive/non-colored cells are counted in each* 4×4 *corner square.*

the cells to bind to the coverslips by covalent bonds. A total of 46 TESPA coated coverslips were prepared according to the protocol in Appendix A.1.1.

In order to stain the cell for colocalization analysis, fluorescent tags were added to specific molecules in the plasma membrane. This is achieved by either adding a fluorophore conjugate molecule which bind directly to a membrane protein, or by immunofluorescence staining, where a primary antibody binds to the target protein. The fluorphore is attached to a secondary antibody, which binds to the primary antibody. In total three fluorphores were used to stain the membrane and two molecules. Because of the time frame of the project the materials were limited to those already available in the lab. This included the membrane dyes C-Laurdan, DiI and DiO, CT-B conjugate with fluorophores Alexa Fluor-647 and Alexa Fluor-594, the primary antibodies CD3 and CD59, and secondary antibodies conjugate with Alexa Fluor-405, Alexa Fluor-488, Alexa Fluor-594 and Alexa Fluor-647. To minimize the effect of chromatic aberration between the two species, fluorophore combinations on the opposite side of the spectrum were avoided.

For the first trial, the membrane proteins CD-3 was used as target proteins for immunofluorescence staining as they are both present in the T-cell receptor complex involved with the antigen recognition of a T-cell mediated immunoresponse [23]. The primary and secondary antibodies used came from mice and rabbits respectively. The second fluorophore is conjugate to the molecule called CT-B, the B sub-unit of cholera toxin, which binds to the membrane ganglioside GM_1 [24]. CT-B can bind up to five GM_1 sites at once and by the addition of an antibody which binds to the CT-B, the bound CT-B molecules are crosslinked, creating lipid rafts [24]. Previous studies have found that T-cell receptors can be found in these lipid rafts, and it is therefore safe to assume that CD-3 colocalizes with GM_1 [6, 7]. Finally the a membrane is tagged with a membrane marker called C-Laurdan, a successor to the membrane marker Laurdan. Laurdan consists of a hydrophobic lauric acid tail which inserts itself into the inner, hydrophobic part of the lipid bilayer, and an omatic ring at the hydrophillic interface with the surrounding [25]. Laurdan is sensitive to the polarity of its environment, and is therefor commonly used to study different lipid phases in lipid bilayers. The abundance of polar watermolecules at the hydrophillic interface in the liquid disorder lipid phase cause Laurdan to react to the dipolar relaxation, leading to a red shift in the emission spectrum ($\sim 440\,\text{nm} \rightarrow 490\,\text{nm}$) [25]. For this project C-Laurdan is used simply as a membrane marker, because of its

low emission wavelength, disregarding its properties as a lipid phase probe. However, because C-Laurdan is commonly used to study lipid phases in membranes, it is known that it is impartial to whether it resides in the liquid ordered or disordered phase. This is a particularly important property when studying colocalization using lipid rafts.

The three fluorophores were chosen as tags based on their fluorescent properties to maximize emission while minimizing the fluorescent overlap - Alexa fluor-488 for the immunofluorescence staining, Alexa fluor-647 for cholera toxin and C-Laurdan for the membrane. The excitation and emission spectra for the first two fluorophores are presented in figure 3.2. C-Laurdan is a relatively new fluorophore, and exact data for its excitation and emission spectra is not readily available, and may instead be seen in figure 3.3. The three fluorophores may be excited by common lasers at wavelength 488 nm, 640 nm and 405 nm respectively.

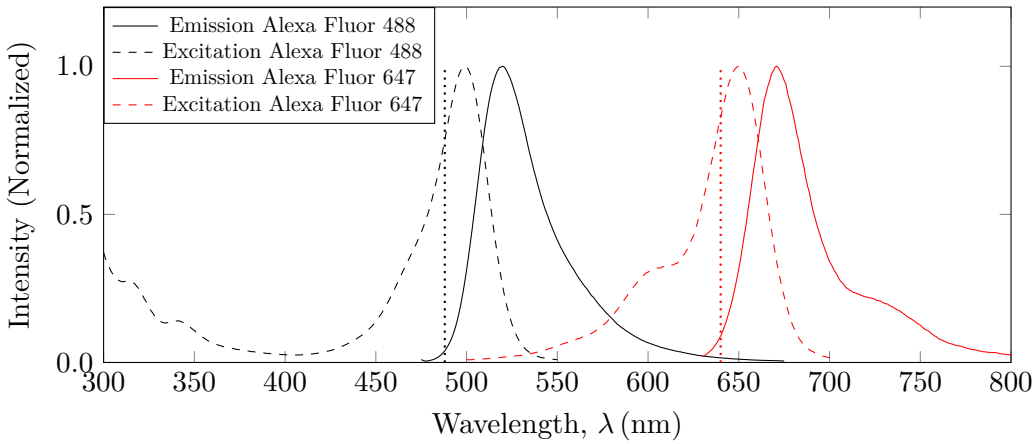

Figure 3.2: *Excitation (dashed) and emission spectra of the fluorophores Alexa fluor-488 (black) and Alexa fluor-647 (red), together with the lines of their respective excitation laser (dotted at* 488 nm *and* 640 nm*)[26].*

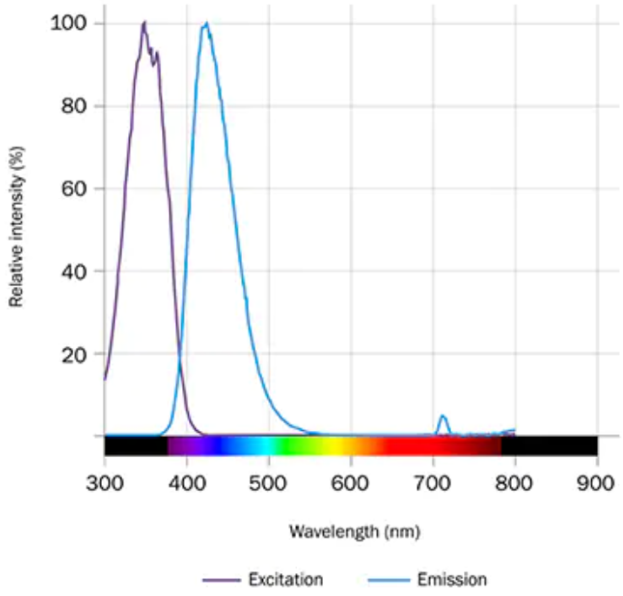

Figure 3.3: *Excitation (violet) and emission (blue) spectra for C-Laurdan [27].*

The membrane and GM_1 receptors were both stained before fixation to keep the membrane as undisturbed as possible, while antibody staining was performed after fixation, a process with the aim to preserve the form and life-like properties of a cell. The cells were fixed using 4% paraformaldehyde (PFA)/PBS, which by crosslinking molecules fixes them in place in the membrane [28]. PFA creates covalent bonds between molecules, effectively attaching them in a network, causing the membrane to harden [28]. The fixed and stained cells were mounted on a glass slide using CitriFluor™AF1 for oil immersion imaging, and sealed with nail polish before being stored in darkness in the refrigerator at 4 °C. The complete protocol for staining can be found in appendix A.1.2.

Early images as seen in figure 3.4 showed problems with both the C-Laurdan staining and the immunofluorescence staining of CD3. The C-Laurdan staining was very weak, but with membrane staining early on in the protocol, before fixation and several steps of washing, it is possible that some fluorescence may have been washed away. To compensate for this, additional membrane staining was added at the end of the protocol, after staining with antibodies. The same set of images showed that the α(anti)-CD3 antibodies were inside the cell, not staining any of the plasma membrane. Why this happened is unknown, but several independent stainings with using different alliquots of α-CD3 gave similar results. It was concluded that the CD3-antibodies were unusable for the purpose of colocalization analysis in the plasma membrane, and another antibody should be used for the immunofluorescence staining.

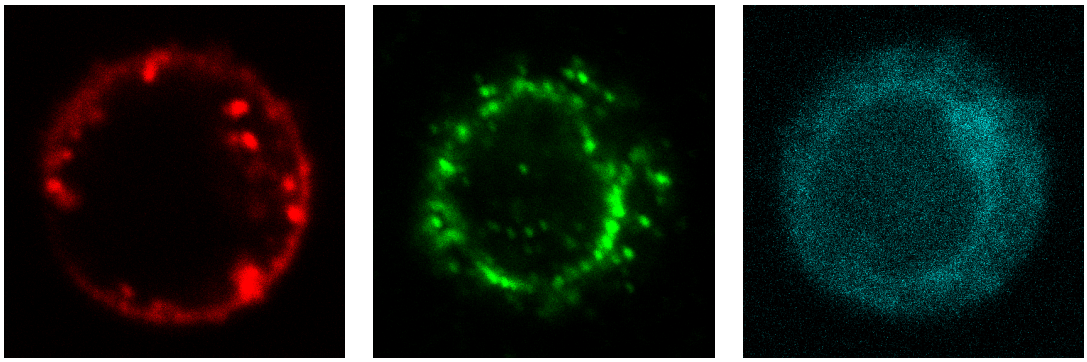

(a) *CT-B conjugate with Alexa Fluor-647*

(b) *CD3 marked with Alexa Fluor-488 only labelling internal membranes.*

(c) *Weak C-Laurdan staining.*

Figure 3.4: *Staining of a Jukrat T-cell with three labels according to the first staining attempt. The fluorophore Alexa Fluor-647 conjugate to the molecule CT-B (a), Alexa Fluor-488 marking the T-cell receptor protein CD3 (b) and the membrane marker C-Laurdan (c).*

For the second trial, 200 µL additional C-Laurdan was added at the end of the protocol with hope of increasing the background signal. The antibody for immunofluorescence staining was exchanged for an antibody which bind to the membrane anchored protein CD59. CD59 is expressed by almost all cell types and is known to play a role in T-cell signaling by indirect interaction with CD3 [2]. However, images showed no signal from the immunofluorescence staining. Attempts were made with higher concentration of secondary antibody, different alliquots and different fluorophore conjugates with no difference in results. It is plausible that the primary antibodies were defective, as opposed to some problem with the fluorophores or secondary antibodies as first suspected.

A third trial was performed, again with target molecules CD59 and GM_1. Instead of

labelling CD59 with a primary, followed by a secondary antibody, the fluorophore was conjugate directly with the primary antibody. Again, CT-B was used for labelling of the GM_1 receptor, with cross-linking to produce patches of lipid rafts. Keeping the same fluorophore combinations as previously, the primary antibody (α-CD59) was conjugate with Alexa Fluor-647, CT-B with Alexa Fluor-488 and the membrane was dyes using C-Laurdan.

A fourth trial was performed using CT-B Alexa Fluor-488 conjugate for GM_1 receptor as target, and α-TfR Alexa Fluor-647 conjugate. α-TfR is an antibody targeting the Transferrin receptor (TfR), a protein tasked with regulating the intake of iron into the cell. Previous studies show that TfR is consistently not fount in GM_1-enriched domains such as lipid rafts, and do not colocalize with CT-B patched lipid rafts [1, 29]. Again, C-Laurdan was used as membrane dye.

3.1.3 Image Acquisition

Images were acquired by *confocal laser scanning microscopy* (CLSM), a fluorescence imaging technique which principle is described in figure 3.5. In CLSM, a laser beam is focused on the specimen, exciting the fluorophores in that specific location. The fluorescent light from the samples fill the entire cone of illumination in the microscope and the specimen is imaged through a pinhole.

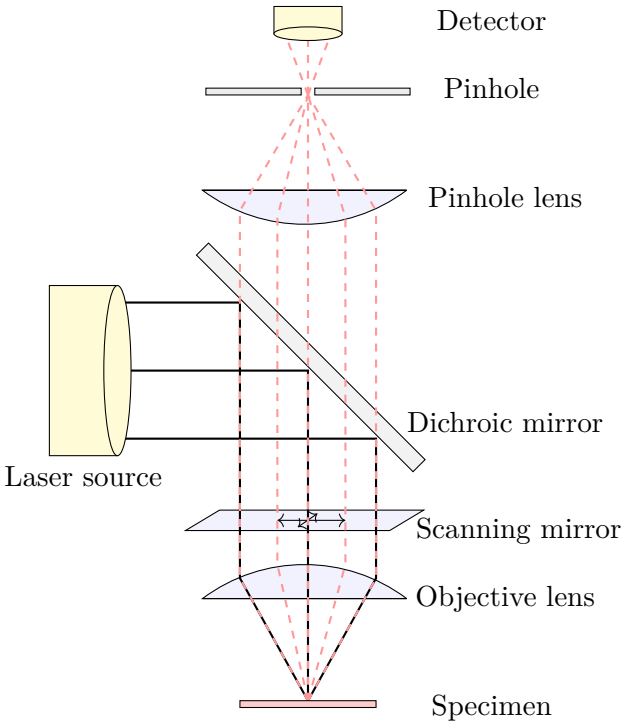

Figure 3.5: *Beam path in a confocal microscope where the condenser lens and the objective lens is one and the same. The beam from the laser (black) is reflected on a dichroic mirror onto the objective lens, focusing it on the specimen. The emitted light from the fluorescent specimen pass through the dichroic mirror and is passed through a pinhole onto the detector.*

When studying several channels at once, it is important to filter the light correctly to minimize cross-talk between the channels. As seen in figure 3.2, the fluorophore Alexa Fluor 488 has a wide excitation spectrum, and will thus be excited by the laser at 405 nm, as well as the emission of C-Laurdan. Thus, when studying the emission of C-Laurdan, the fluorescent light from Alexa Fluor 488 must be removed from the signal. In the confocal microscope this is achieved by the use of dichroic mirrors, which reflect certain wavelengths while letting other pass through, effectively filtering the light. The confocal fluoprescence microscope at our disposal was equipped with a secondary variable dichroic filter, resulting in a free choice of filtering wavelengths. This principle is shown in figure 3.5, which shows the path of both the laser beam and the emitted fluorescent light. The laser is then swept over the image by the use of scanning mirrors, exciting the fluorophores at one location at a time. As the emitted light from all locations are gathered, a high resolution image of the specimen is acquired.

The confocal microscope used for the image acquisition was ZEISS LSM 700 monitored by the software ZEN. The microscope has four lasers (405 nm, 488 nm, 561 nm and 647 nm), 4 objectives (10× air immersion, 20× air immersion, 40× oil immersion, 63× oil immersion), and a variable secondary dichroic mirror for optimal filtering of the emitted signals. The images were acquired using sequential imaging (one channel at a time) using excitation lasers 405 nm for C-Laurdan, 488 nm for Alexa Fluor-488 and 647 nm for Alexa Fluor-647. In order to minimize cross-talk and bleed-through emission filters were set to 500 nm for both C-Laurdan and Alexa Fluor-488. For maximum magnification and optimal resolution an objective with 63× magnification with 1.4 oil immersion (numerical aperture $NA = 1.4$), was used and the pinhole size was set to 1 AU (airy unit) for the largest wavelength (647 nm).

3.2 Simulations

A foundational assumption in colocalization analysis is the uniformity of the background, the plasma membrane on which the molecules of interest reside. In this chapter, we will simulate the consequences when this assumption is violated. We imagine a non-flat plasma membrane, where convolutions and folding create an inomogeneous distribution of membrane. For the simulations this is realized as an image with varying intensity, where high intensity indicated a higher concentration of plasma membrane and low intensity indicates a lower concentration of membrane. This background is then, later in the simulations, used for the normalization by weighting the observations in each pixel with the corresponding background intensity. The molecules of interest are modelled by randomly distributing points on this background, as inspired by the method of [15], with greater probability of finding a point where the background intensity is larger. Given that the molecules are uniformly distributed on the membrane, more membrane will contain more membrane molecules.

The simulations made to investigate the effect of background normalization on two samples following a background distribution, are modelled by variations of inhomogeneous Poisson processes. A Poisson process is a spatial point process X on a set $A \in \mathbb{R}$, as described in section 2, on a set $B \subseteq A$, and $X(B)$ is the number of points is X which belong to B. A process is *stationary* and *isotropic* if it is invariant to translation and rotation on the subset B [30]. For one such point process it can be shown that

$$\mathbf{E}[X(B)] = \lambda|B|, \tag{3.2}$$

where λ is called the intensity of the process. A Poisson process on B with intensity λ is defined as

$$\mathbf{P}(X(B) = n) = \frac{(\lambda|B|)^n}{n!} e^{\lambda|B|}, \tag{3.3}$$

and is both stationary and isotropic [30]. Furthermore, an inhomogeneous Poisson process has a varying intensity described instead by the function $\lambda(x, y)$.

The first set of simulations consisted of $n = 500$ samples with inhomogeneous intensity functions $\lambda_1(x, y)$ and $\lambda_2(x, y)$ where $\lambda_i(x, y) = \exp(l_i(x, y))$ and l_i are the backgrounds generated by

$$l_1 = 1 - \log(x + 1), \tag{3.4}$$

$$l_2 = 1 - (\log(x + 1) + \log(y + 1)), \tag{3.5}$$

respectively as seen in figure 3.6a and 3.6b. The second set of simulations were conducted using a Log-Gaussian Cox process, a hierarchic stochastic model, realized by an inhomogeneous Poisson process $Z|X$, with intensity $\lambda(x, y) = \exp(X(x, y))$, where X is a Gaussian random field [31]. A Gaussian random field of size 100×100 was simulated with mean $\mu_s = 1$ and Matérn covariance function

$$C(d) = \frac{\sigma^2}{2^{\nu-1}\Gamma(\nu)} (\kappa d)^\nu K_\nu(\kappa d), \tag{3.6}$$

where d is the distance between two points, σ is the variance, $\Gamma(\nu)$ is the gamma function, K_ν is the modified Bessel function and ν and κ are parameters deciding the smoothness and correlation length. In all simulations $\sigma^2 = \kappa = \nu = 1$ was used, and one such simulation can be seen in figure 3.6c. For future reference, the background images in figure 3.6 will be called B_1, B_2 and B_3 for figure 3.6a, 3.6b and 3.6c.

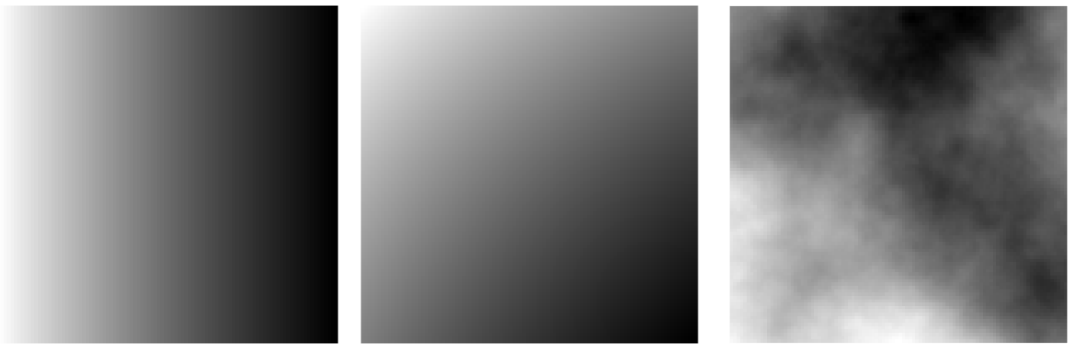

(a) *Simulated background intensity according to* $l_1 = 1 - \log(x + 1)$.

(b) *Simulated background intensity according to* $l_2 = 1 - (\log(x + 1) + \log(y + 1))$.

(c) *Simulated Gaussian random field with Matérn covariance function with* $\sigma^2 = \kappa = \nu = 1$.

Figure 3.6: *Simulated backgrounds for point processes simulations.*

Points for two samples of the same size were generated according to the two methods. The samples were created with varying degree of independence by generating the first sample, S_1, and then using various amounts of S_1, with some small displacement $\varepsilon \sim \mathcal{N}(S_1^i, \sigma^2)$ as part of the second sample, S_2. These proportions, p, were varied between

0 and 1, where $p = 0$ represent two independent samples and $p = 1$ uses the entire sample S_1 as basis for sample S_2. When $p \neq 1$ the remaining samples of S_2 were sampled independently.

In order to simulate the process of image acquisition from a fluorescence microscope, the limited resolution and optical filtering, the intensity of each point was spread by a point spread function by 2D convolution of a Gaussian smoothing kernel according to eq. (2.2), much like the PSF is convoluted with the emitted light in the imaging system. The complete simulated signal was then normalized to grayscale (0-1). Three simulations can be seen in figure 3.7. Each simulation is of size 100×100 pixels and contains two independent ($p = 0$) species (green and red) with sample size $n = 1000$ on the backgrounds B_1, B_2 and B_3 in figure 3.6.

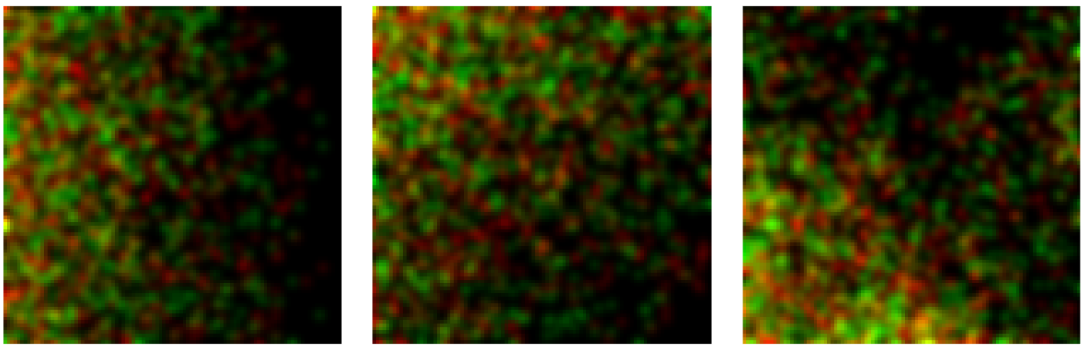

(a) *Two independent point process with background according to* B_1.

(b) *Two independent point process with background according to* B_2.

(c) *Two independent point process with background according to* B_3.

Figure 3.7: *Two independent point process (green and red, sample size* $n = 1000$*, collocation proportion* $p = 0$*) with intensity according to* $\lambda = \exp(l(x, y))$*, where* l *is the intensities in figure 3.6.*

The correlation between the two signals is estimated by the Pearson correlation coefficient and Spearman rank correlation coefficient. Correlation coefficients were calculated only on pixels with non-zero signal after filtering in both channels/species, and by doing so excluding background and non-overlapping intensities. The simulations were conducted 100 times for each intensity λ_1, λ_2 and the Gaussian random field, after which the difference between the mean correlation coefficients before and after division with the background were investigated. The difference was confirmed using a Student's t-test, with null hypothesis of no difference. The Student's t-test is a hypothesis test where the test statistic is, under the null hypothesis, assumed to belong to a Student's t-distribution. For the testing of difference between two samples A and B of size n_A and n_B, the test statistic can be written as

$$t = \frac{\bar{A} - \bar{B}}{\sqrt{\frac{s_A^2}{n_A} + \frac{s_B^2}{n_B}}}, \tag{3.7}$$

where s_A and s_B are their standard deviations. This is then compared to a tabulated value based on significance level, to determine whether the null hypothesis is accepted or rejected.

3.3 Image Analysis

The images produced by confocal microscopy were analysed with a combination of software. The Fiji version of ImageJ was used mainly for file conversion and selection of the region of interest, while MATLAB was used for the image processing and the image and colocalization analysis.

3.3.1 Images Processing

The images produced by the microscope are 16 bit images of the format `.lsm`. The images were converted to `.tif` format, in order to work with them in non-system-specific software such as MATLAB. The conversion was done using the ImageJ function `batch > convert` with bilinear interpolation, scale factor 1.00 and option "Read image using bioformat" checked. The resulting images were 8 bit image stacks of format `.tif` where each slice in the image stack corresponds to one channel. These images were used for all of the following processing and analysis.

When working with several fluorescence signals at once, it is important to remember that fluorophores have different fluorescent properties, and such the recorded intensity is not immediately comparable between the channels. The emitted fluorescence intensity is also dependent on the intensity of the excitation beam. The laser intensity may vary in different channels due to difference in fluorophore properties which cause saturation of the detector at different excitation intensities. In order to compare the channels despite their difference in intensity distribution, the intensity of each channel is adjusted by converting each channel to gray-scale, resulting in maximum intensity = 1 and minimum intensity = 0 for each channel.

After adjusting the intensity of the three channels a background subtraction was performed in order to reduce some noise. A window without any signal was picked for each image, and the mean value of this window was subtracted from every pixel.

Due to chromatic aberration in the acquisition, there may be some shift between the channels. To adjust for this, the image slices containing each channel were aligned using image registration, provided by the function `Align_slices in stack` in the ImageJ plugin `Template matching`.

3.3.2 Region of Interest

The plasma membrane is the thin, outermost lipid bilayer of the cell, and is approximately spherical for the Jurkat T-cell. The lipid bilayer of the plasma membrane has a thickness of approximately 5 nm, while an image from a confocal microscope has a pixel size of approximately 100 nm. Aiming to include only the plasma membrane when selecting the region of interest, the resulting ROI is a one pixel wide line along the plasma membrane. The ROI was selected by manually selecting the brightest pixel around the edge of the cell.

With a PSF with full width half maximum of approximately 400 nm some information is lost using this approach, due to the spreading of signal to neighbouring pixels. However using a wider ROI, for example by thresholding as outlined in section 2, might include signal from objects very close to the membrane such as vesicles for endocytosis and exocytosis. On the other hand, noisy signals can make it difficult to choose the pixel where the membrane is located, especially in combination with signals close to the membrane. To lessen the effect of this, an estimated value was used instead of the true pixel value at the ROI. In order to take the surrounding values into account an estimation of the pixel value

on the ROI was made by taking the mean of each three-by-three pixel neighbourhood. This estimation was realized by filtering using 2D-convolution according to equation 2.3, using a 3×3 average kernel

$$h = \frac{1}{9}\begin{pmatrix} 1 & 1 & 1 \\ 1 & 1 & 1 \\ 1 & 1 & 1 \end{pmatrix}. \tag{3.8}$$

3.3.3 Gaussian Process Interpolation

As mentioned, intensity based measures of colocalization are highly sensitive to noise. When conducting analysis on a ROI only one pixel wide, the sensitivity increases even further as it is difficult to determine whether the value of a pixel is due to signal or due to noise. To minimize the impact of noise, we assume that any signal variance lower than $\sigma = 0.05$ is due to noise. The true signal is estimated by means of interpolation of the intensity distribution in each channel. Our choice of method of interpolation is Gaussian process regression along the manually segmented ROI. For the GPR modelthe pixel intensity values on the ROI are used as observations and the pixel indices along the ROI as predictors. The GPR was conducted using the MATLAB function `fitrgp` with Matérn covariance function, constant basis function and constant standard deviation $\sigma = 0.05$ of the noise. An example of a GPR fit can be seen in figure 3.8b to the intensity of a one pixel wide ROI of the simulated cell 3.8a.

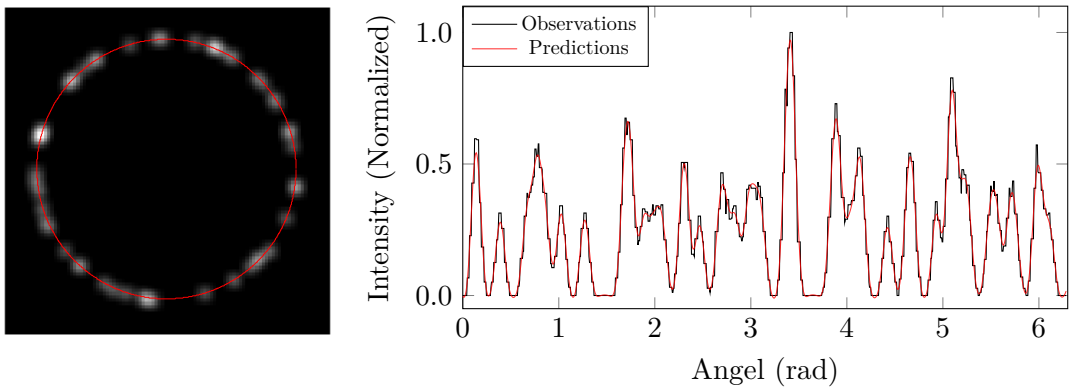

(a) *Simulated cell ($n = 50$), with one pixel wide ROI (red).*

(b) *Intensity profile of cell along ROI in (a) (black), GPR interpolation of the intensity profile (red).*

Figure 3.8: *Example of GPR interpolation as means of noise reduction.*

4 Results

4.1 Simulations

Simulations were produced according to the methods described in section 3.2. The result of three simulations (sample size $n = 1000$) of two independent species on backgrounds B_1, B_2 and B_3 (see figure 3.6), are presented in figures 4.5, 4.6 and 4.7 respectively, together with their corresponding intensity scatter plots. For all three simulations one can by visual inspection see that the normalized image appears more homogeneous in its intensity distribution compared to the original. Comparing the intensity scatter plots before and after normalization (figures 4.5-4.7b and d) it is clearly visible how the normalization has decreased the ellipticity of the point scatter and equivalently the correlation between species. This is an indication of uniform intensity distribution and can be compared with the corresponding simulation on a uniform background in figure 4.8. The more homogeneous intensity distribution is confirmed by the correlation coefficients before and after normalization. For example for the simulation in figure 4.6 the calculated correlation coefficients are $\rho_p = 0.3925$, $\rho_s = 0.3936$ before and $\rho'_p = 0.0461$, $\rho'_s = 0.0544$ after normalization, where ρ_p is the Pearson correlation coefficient and ρ_s is the Spearman rank correlation coefficient. Figure 4.1 presents the mean correlation coefficients with respective standard deviation of $N = 100$ independent simulations, before and after background normalization.

As expected, after normalization, the correlation coefficient between each signal and the background is significantly decreased, indicating a successful reduction of each signal's dependency on the background. A two tailed t-test of the difference before and after normalization was conducted for each set of correlation coefficients. The test confirmed a significant difference at significance level $\alpha = 0.05$, between the correlations before and after normalization, both between the species and also between each species and the background.

The impact of background normalization on the correlation coefficients was studied further by conducting $N = 100$ independent simulations for all combinations of 11 collocation proportions ($p = 0, 0.1, ..., 1$) and 13 sample sizes ($n = 100, 250, 500, 750, 1000, 1500, ..., 5000$). The mean Pearson correlation coefficient of these simulations on backgrounds B_1, B_2 and B_3, may be seen in figures 4.10, 4.11 and 4.12 respectively. For comparison, the results from corresponding simulations on a uniform background is presented in figure 4.9.

4.1.1 Impact of Sample Size

Figures 4.10c and d presents the Pearson correlation coefficient as a function of the sample size, for different collocation proportions. From these figures, it is clear that the correlation coefficient is heavily dependent on sample size. Although the effect of sample size is reduced after background normalization, some dependency remains, and the same effect can be seen for two independent samples on a uniform background in figure 4.9b.

As the sample size increases, the density of species will increase more in areas of high background intensity than in areas of low background intensity. This will lead in larger differences in the species' intensity in these areas, and ultimately result in a higher corre-

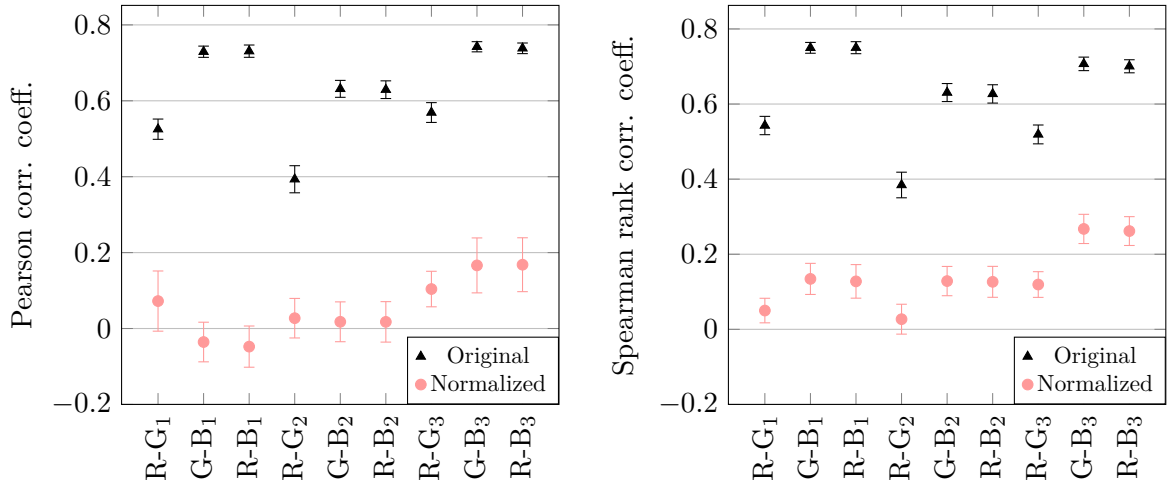

(a) **(b)**

Figure 4.1: *Mean Pearson (a) and Spearman rank (b) correlation coeffiecients and standard deviations ($N = 100$) before (black triangles) and after (red circles) normalization for two independent species (R and G) of size $n = 1000$, with each other and the background, for the backgrounds B_1, B_2 and B_3.*

lation between species. Scatter plots of three simulations with of independent samples of sizes (n =1000, 2500, 5000) on background B_2, before and after background normalization are shown in figure 4.2. In figure 4.2a-c it is clear that there is some dependency which increase with sample size as the scatter plots shape approach a line as sample size increase. After normalization (4.2d-f) the scatter plots show a successful reduction of the dependency, as they have the characteristic round shape associated with independent species on a uniform background. From this one can conclude that the underlying dependency is the background, and this is reduced when normalizing, independent of sample size.

The correlation coefficients do not follow the same behaviour for very small sample sizes as seen in figure 4.10c. The correlation coefficient is larger for small samples, the smallest in these simulations being 100, before decreasing suddenly before increasing again, creating a kink in the curve around sample sizes of 250. This is most likely an effect of how the correlation calculations are set up. As described in chapter 3, the correlation calculations only take pixels containing signal from both species into account. For very small sample sizes the chance of two non-collocating samples overlapping is very small. Thus, the samples which collocate make out a large part of all the measured signal, resulting in an disproportionately large correlation coefficient. However, with a typical molecule density of $70 - 80\text{molecules}/\mu\text{m}^2$ in the plasma membrane, these low sample sizes are unlikely to appear in a real experiment.

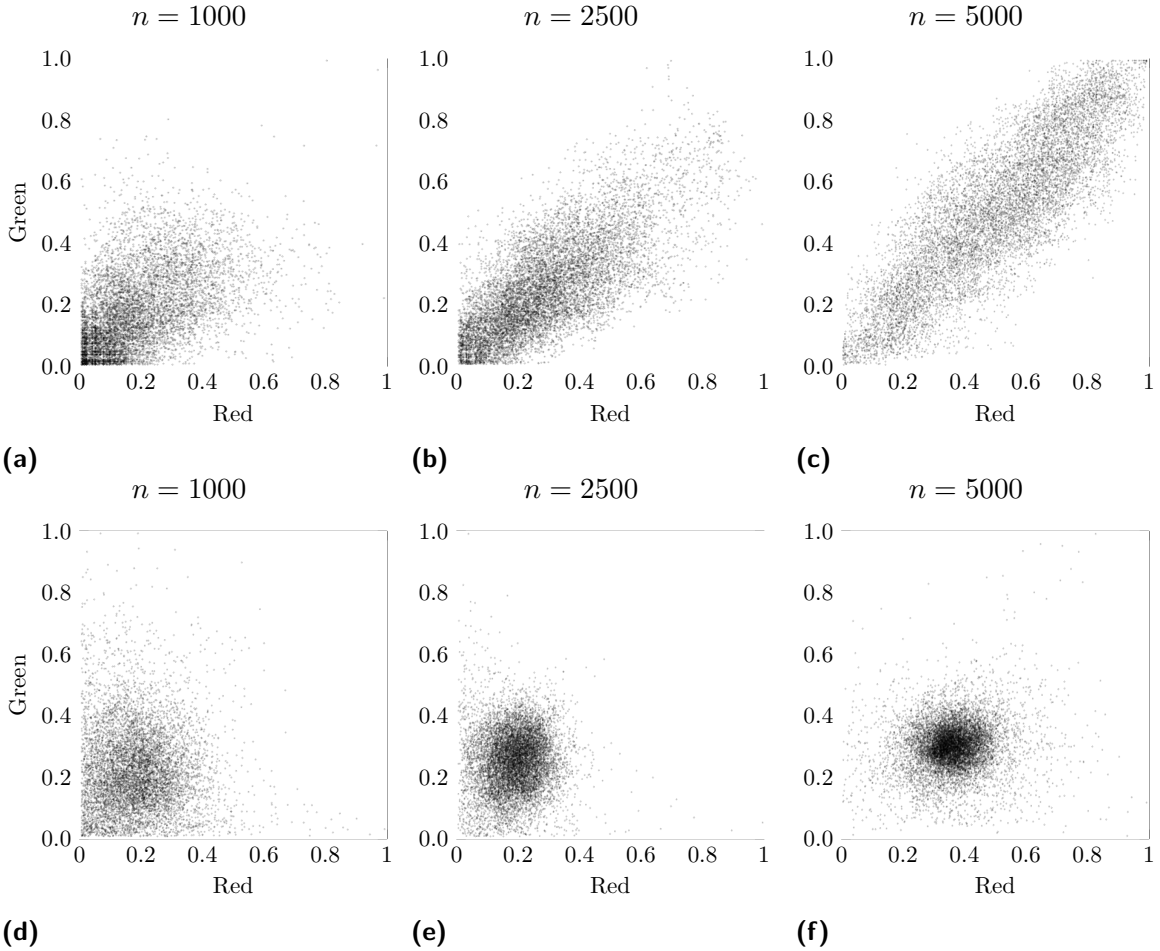

Figure 4.2: *Scatter plots before (top) and after (bottom) background normalization for two independent species on background B_2 for three sample sizes ($n = 1000, 2500, 5000$).*

4.1.2 Comparison of Correlation Coefficients

As mentioned, there is a debate regarding which correlation coefficient to use when conducting colocalization analysis. Figure 4.3 presents the Pearson and Spearman rank correlation coefficients for the same independent samples of size 1000, before and after background normalization, for backgrounds B_1, B_2 and B_3. From visual inspection, there is little difference between the use of the Pearson and the Spearman rank correlation coefficient before normalization. However, after normalization the difference is more pronounced especially in figure 4.3a, as the Pearson correlation coefficient tends to overestimate the correlation whereas the Spearman rank correlation coefficient appears linear. This is confirmed by linear regression of the correlation coefficients after normalization in figure 4.3, presented in table 4.1. Here, the Spearman rank correlation coefficients are closer to that of a simulation on a uniform surface than the Pearson, for simulations on all surfaces. Comparing the Pearson and Spearman rank correlation coefficients after normalization, and their respective slopes in figure 4.3 and table 4.1, it is clear that the largest difference between the coefficients comes from the simulations using B_1 as background. A plausible reason for this is that background B_1 has a larger amount of high and low intensity values than B_2 and B_3, which both have a larger amount of middle range intensity values. After

normalization, the samples in the low intensity area of the background receive a greater weight resulting in high intensity outliers which the Pearson correlation coefficient is more sensitive to than the Spearman rank correlation coefficient.

Table 4.1: *Linear regression estimates and their R^2-values for the Pearson (ρ'_p) and Spearman rank (ρ'_s) correlation coefficient after normalization for varying collocation proportions as seen in figure 4.3, and of two species on a uniform surface with 1000 samples.*

Background	**Coefficient**	**Slope**	R^2
B_1	ρ'_p	0.9075	0.9896
	ρ'_s	0.9526	0.9986
B_2	ρ'_p	0.9749	0.9995
	ρ'_s	0.9768	0.9978
B_3	ρ'_p	0.9016	0.9993
	ρ'_s	0.8866	0.9974
Uniform	ρ'_p	1.002	0.9992
	ρ'_s	0.9994	0.9978

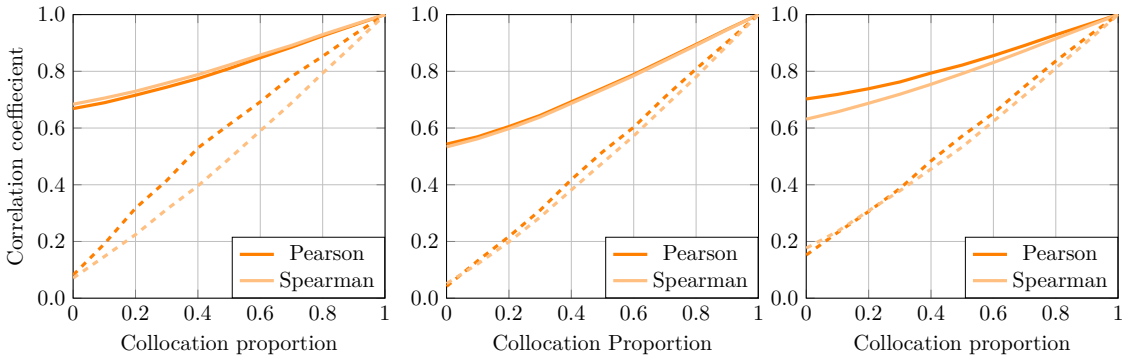

Figure 4.3: *Mean Pearson and Spearman rank correlation coefficient of $N = 100$ simulations of two signals, as a function of collocation proportion before (solid) and after (dashed) background normalization for backgrounds B_1 (a), B_2 (b) and B_3 (c).*

4.1.3 Impact of Correlation With Background

The simulations above are made with the assumptions that the location of a specie is heavily dependent on the background distribution. Figure 4.4 presents the mean correlation coefficient of the case where two species are independently and uniformly distributed over the image, with no dependency on the background. The simulation consists of $N = 100$ simulations of two independently and uniformly sampled species of sample size $n = 1000$, and the background used for weighting is background B_2. In contrast to the results above, we see here that normalizing the intensity of the species with the background intensity creates a strong negative correlation between species and background. Since both species are now dependent on the background, a false correlation has been created between the two.

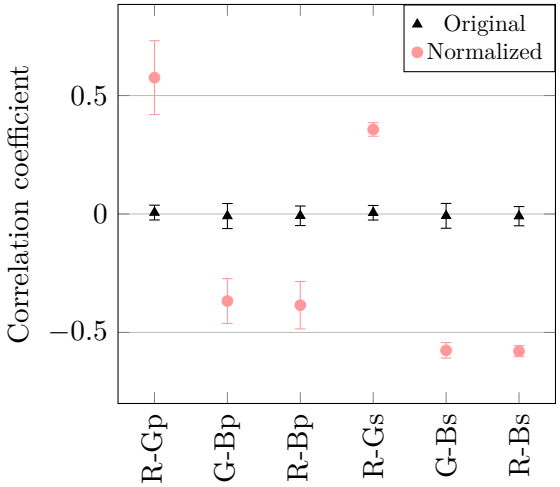

Figure 4.4: *Mean Pearson (p) and Spearman rank (s) correlation coeffiecients and standard deviations ($N = 100$) before (black triangles) and after (red circles) normalization for two independently and uniformly sampled species (R and G, independent of the background) of size $n = 1000$, with each other and background (B) for background B_2.*

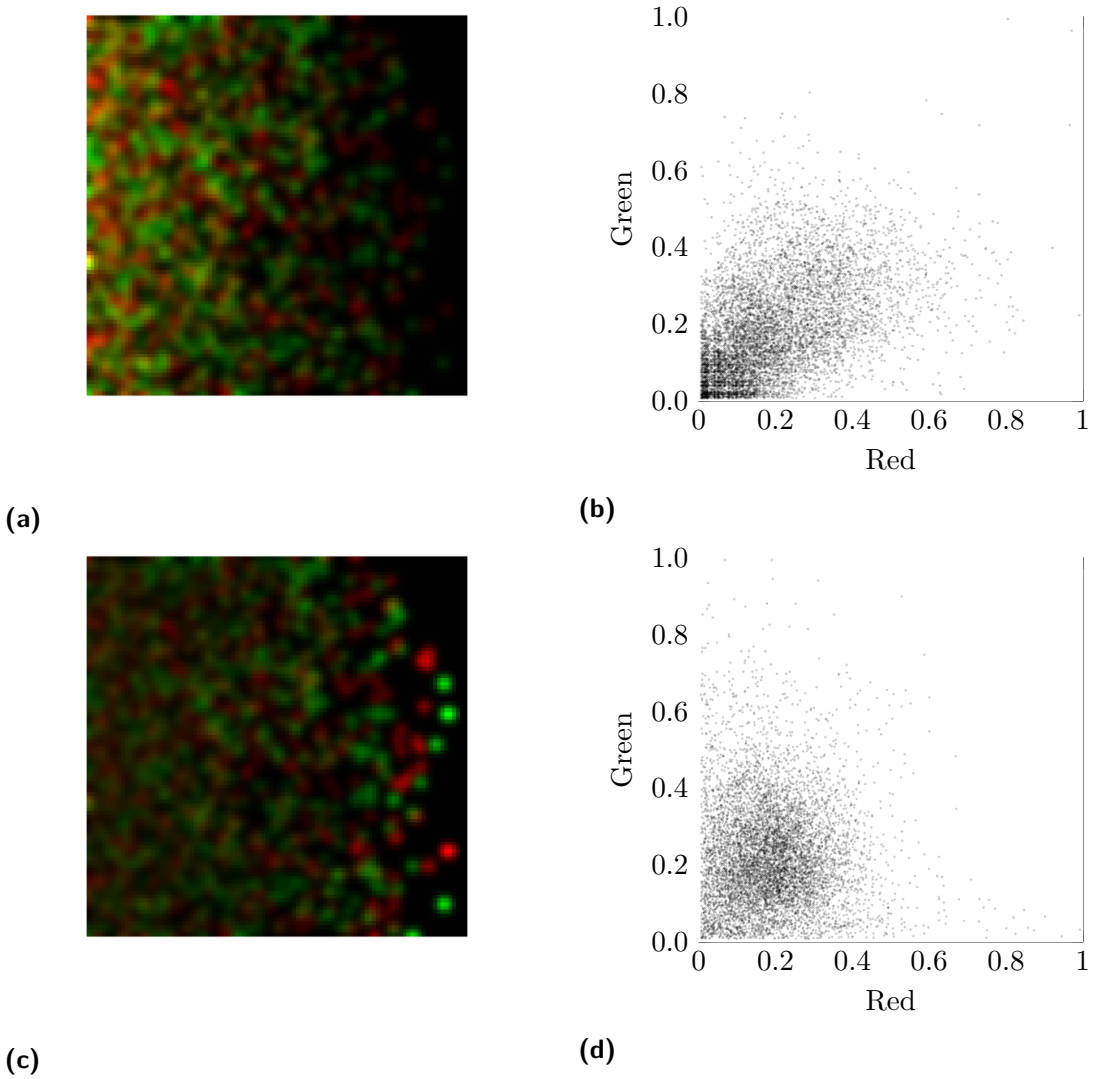

Figure 4.5: *Simulation of two independent species (green and red) on background B_1, before (a) and after (c) background normalization, together with their respective intensity scatter plots (b & d).*

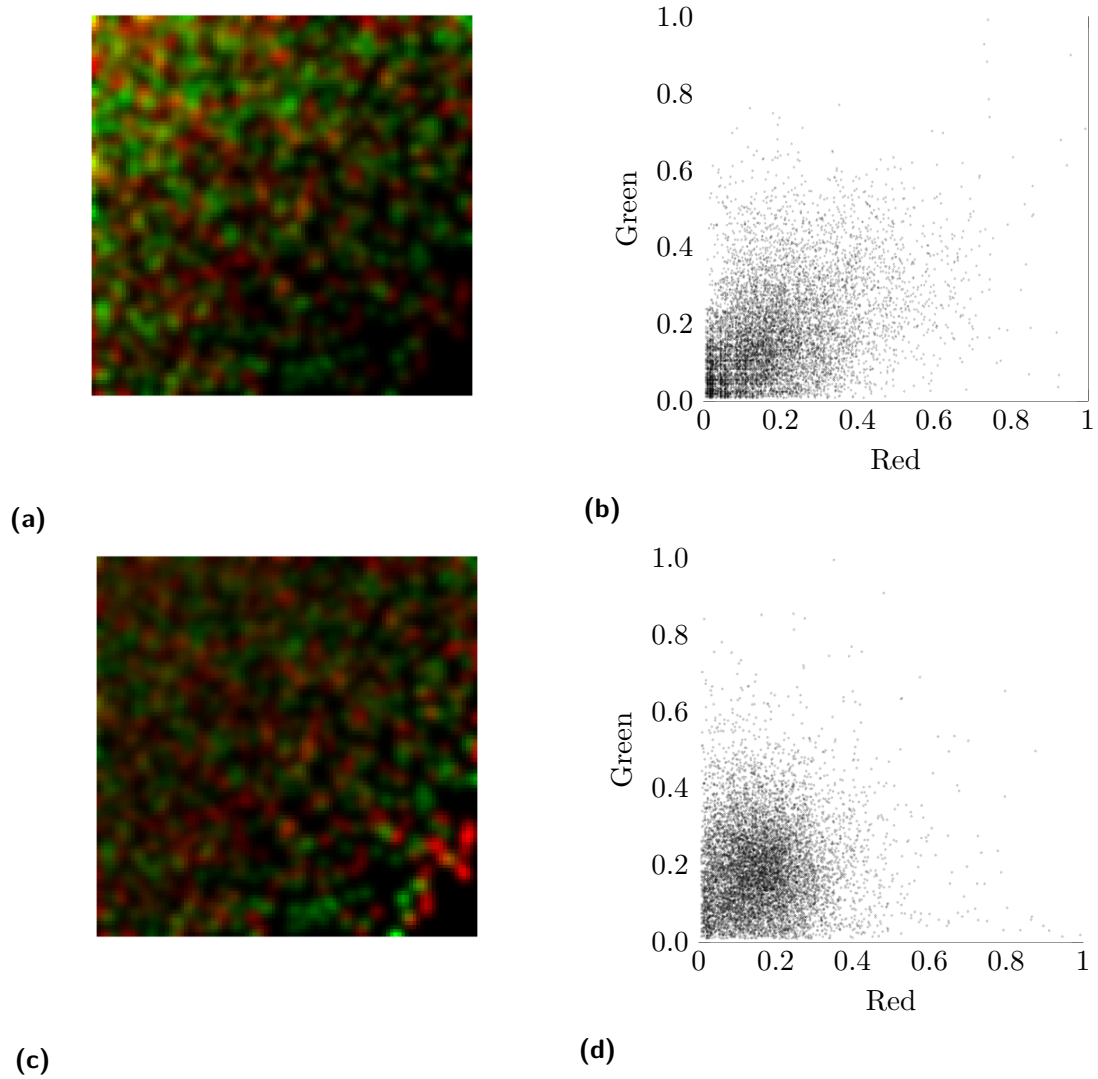

Figure 4.6: *Simulation of two independent species (green and red) on background B_2, before (a) and after (c) background normalization, together with their respective intensity scatter plots (b & d).*

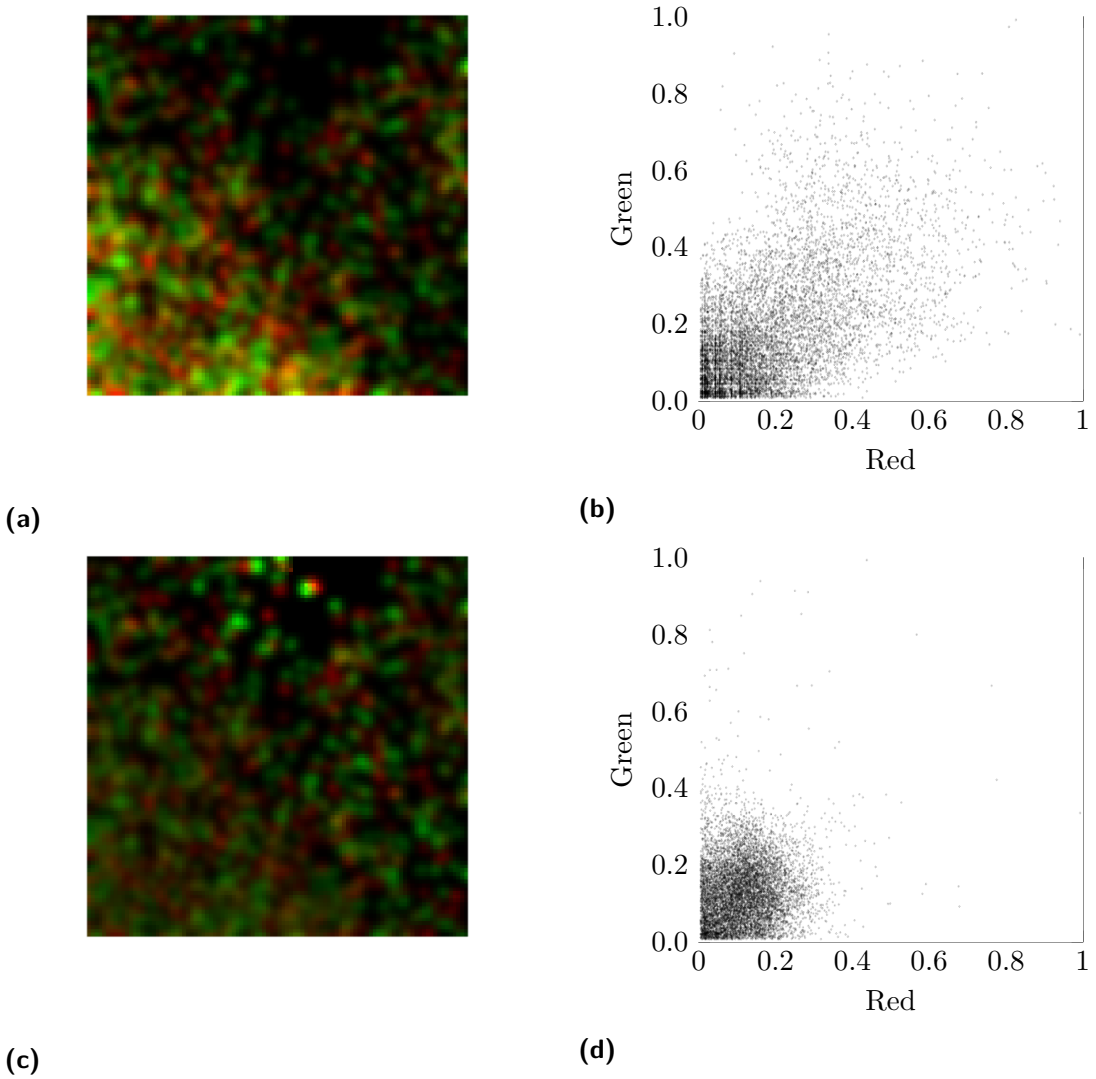

Figure 4.7: *Simulation of two independent species (green and red) on background B_3, before (a) and after (c) background normalization, together with their respective intensity scatter plots (b & d).*

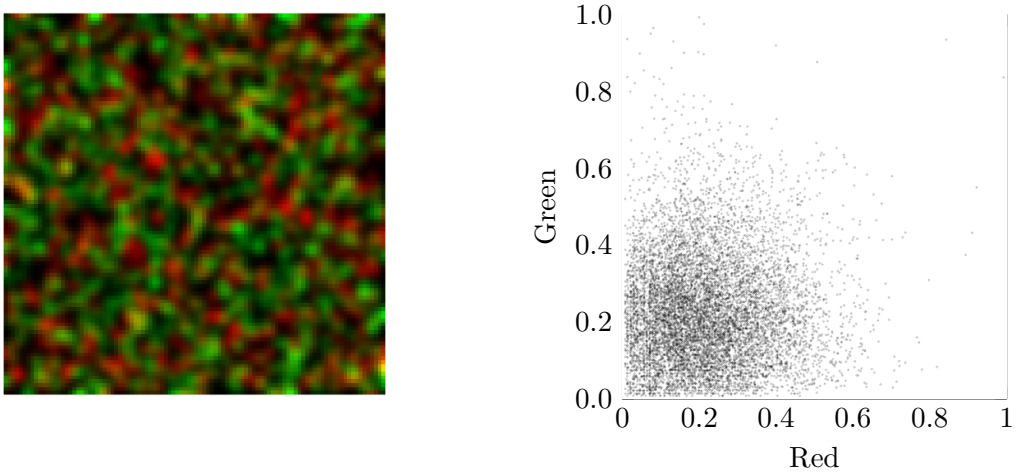

(a) **(b)**

Figure 4.8: *Simulation of two independent species (green and red) on a uniform surface (a), together with the corresponding intensity scatter plot (b).*

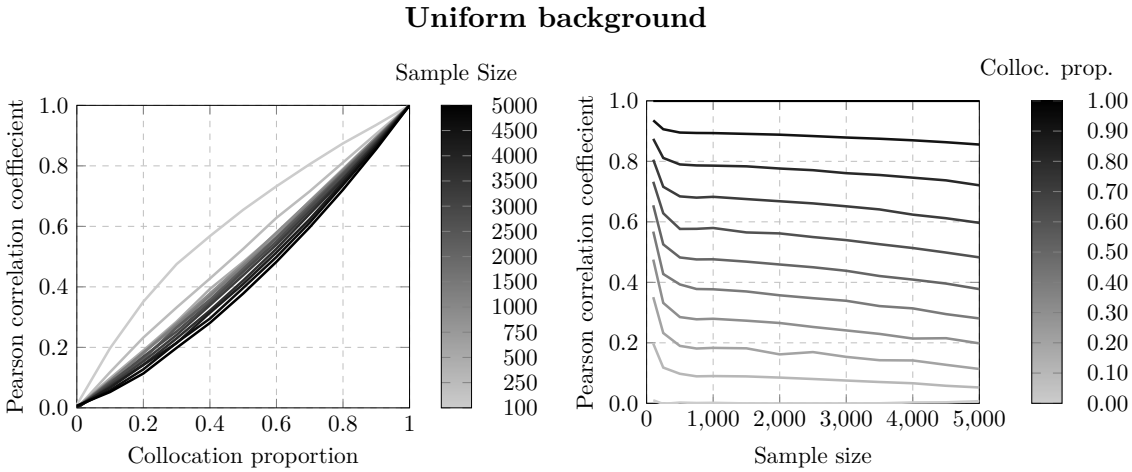

(a) **(b)**

Figure 4.9: *Mean Pearson Correlation coefficient of $N = 100$ simulations as a function of sample size of the sample for varying collocation proportions (a), and Mean Pearson Correlation coefficient of $N = 100$ simulations as a function of sample size of the sample for varying collocation proportions (b), for a simulation on a uniform background.*

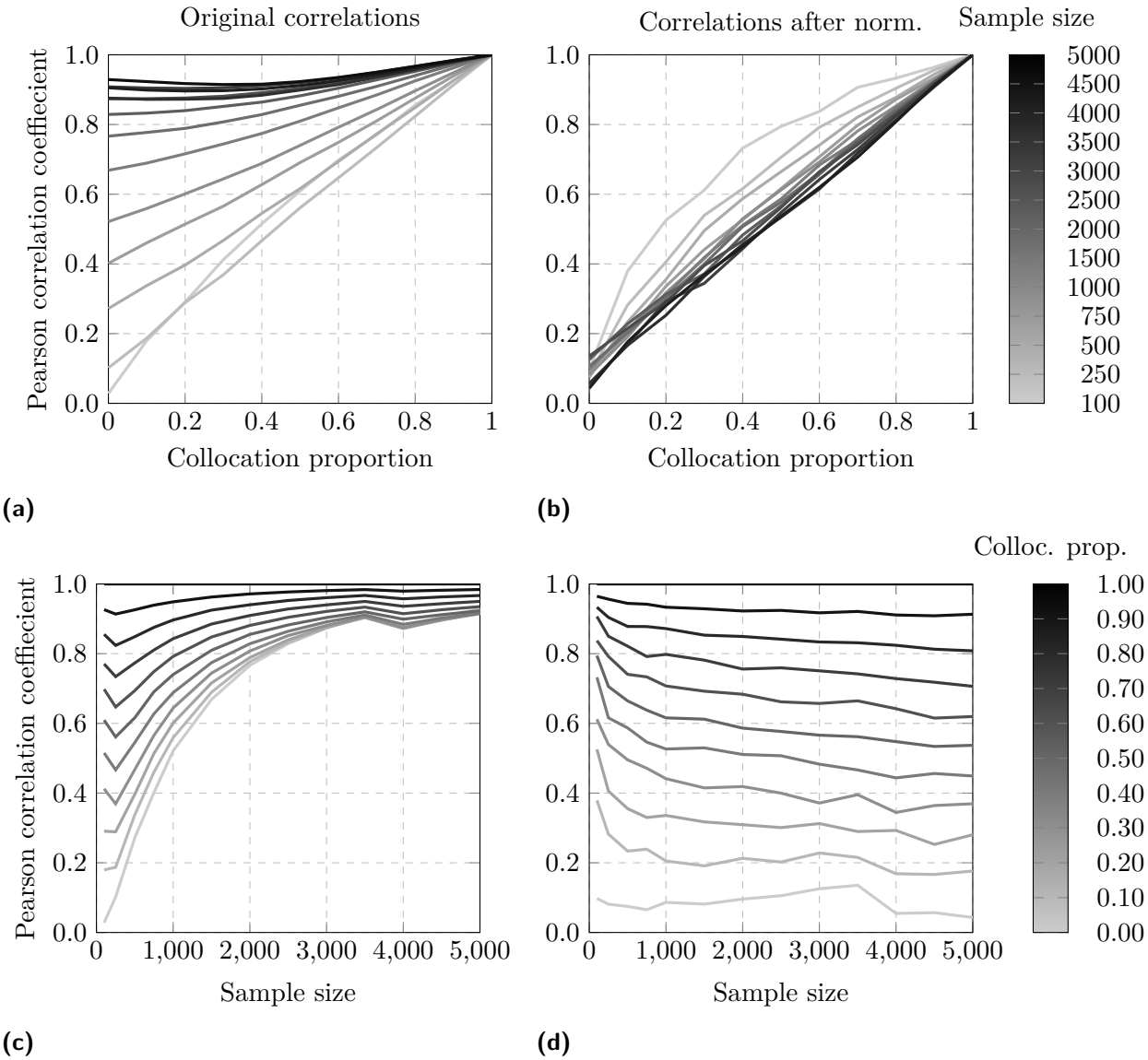

Figure 4.10: *Top: Mean Pearson Correlation coefficient of $N = 100$ simulations on background B_1 before (a) and after (b) background normalization as a function of collocation proportion of the sample for varying sample sizes. Bottom: Mean Pearson Correlation coefficient of $N = 100$ simulations before (a) and after (b) background normalization, as a function of sample size of the sample for varying collocation proportions.*

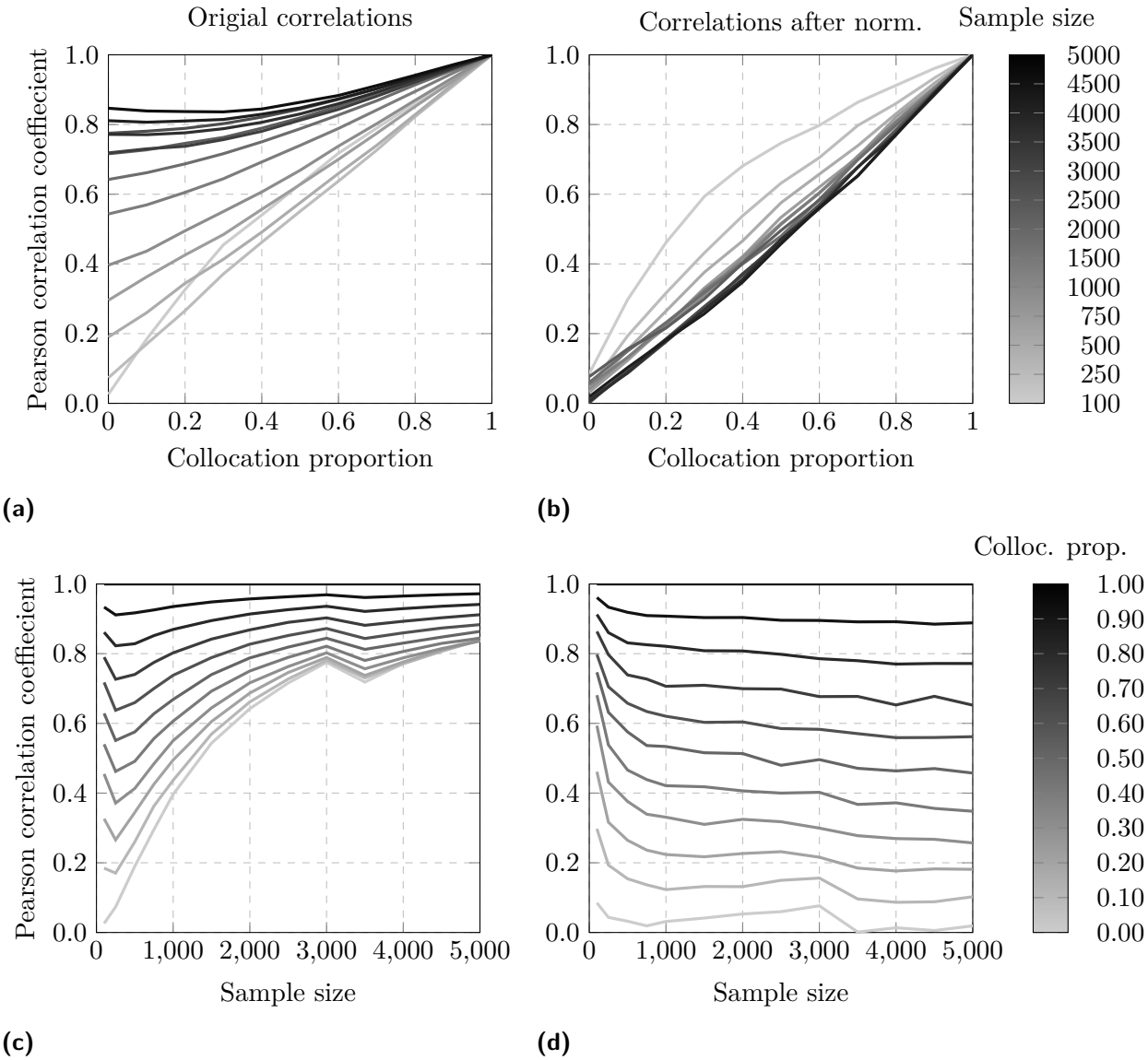

Figure 4.11: *Top: Mean Pearson Correlation coefficient of $N = 100$ simulations on background B_2 before (a) and after (b) background normalization as a function of collocation proportion of the sample for varying sample sizes. Bottom: Mean Pearson Correlation coefficient of $N = 100$ simulations before (a) and after (b) background normalization, as a function of sample size of the sample for varying collocation proportions.*

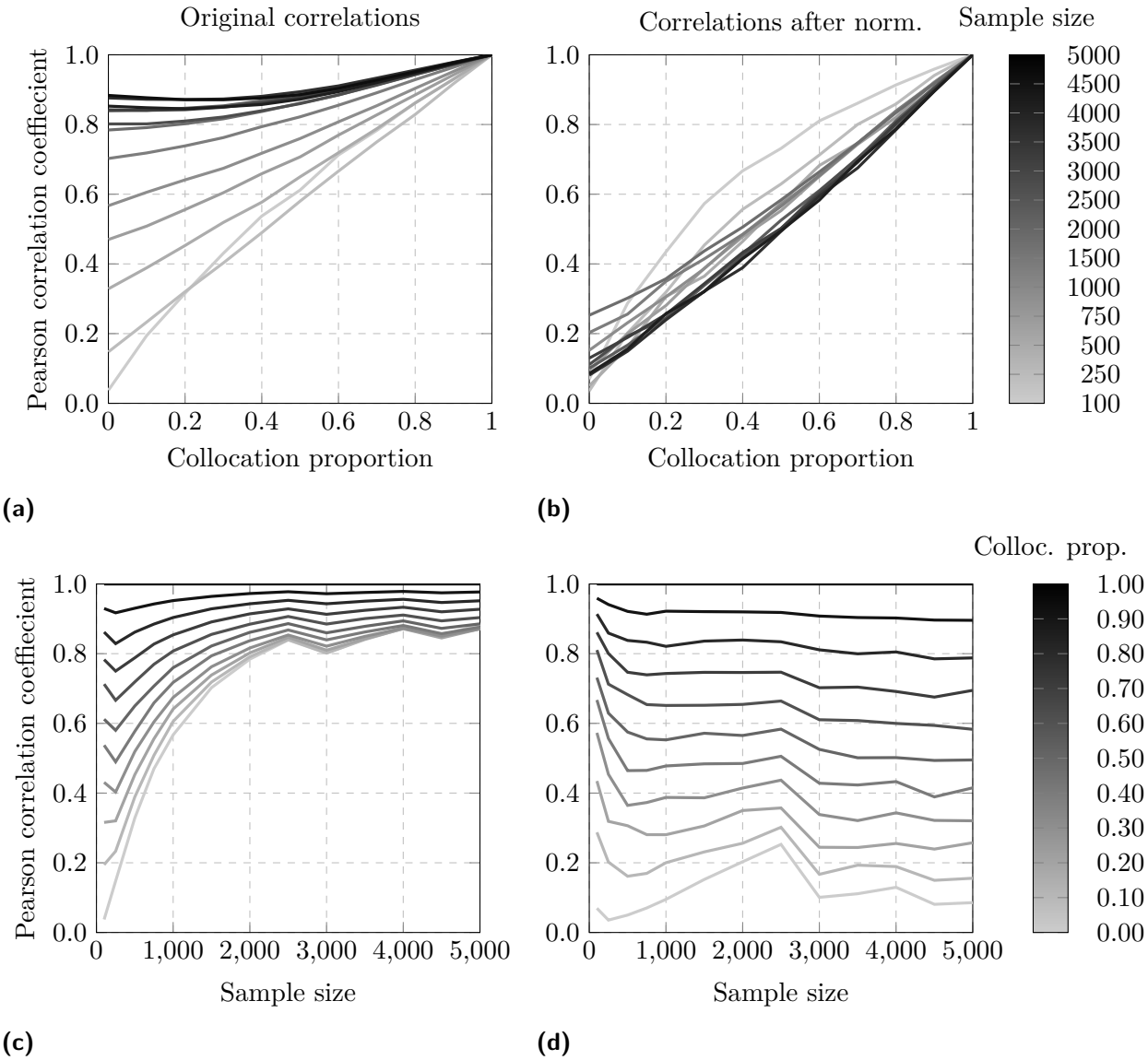

Figure 4.12: *Top: Mean Pearson Correlation coefficient of $N = 100$ simulations on background B_3 before (a) and after (b) background normalization as a function of collocation proportion of the sample for varying sample sizes. Bottom: Mean Pearson Correlation coefficient of $N = 100$ simulations before (a) and after (b) background normalization, as a function of sample size of the sample for varying collocation proportions.*

4.2 Experimental Results

The third and fourth trial of fluorescence staining in section 3.1.2 were considered successful as fluorescence could be found in the membrane in all three channels. Images of the stained cells were acquired according to section 3.1.3, and can be sen in figure 4.13 where CT-B was conjugate with Alexa Fluor-488 and $\alpha-$CD59 was conjugate with Alexa Fluor-647. Figure 4.14 presents a T-cell staining using CT-B Alexa Fluor-488 conjugate, α-TfR Alexa-647 conjugate. As described in section 3.1.2, the CT-B and α-CD59 are expected to collocate, while the combination of CT-B α-TfR are expected not to.

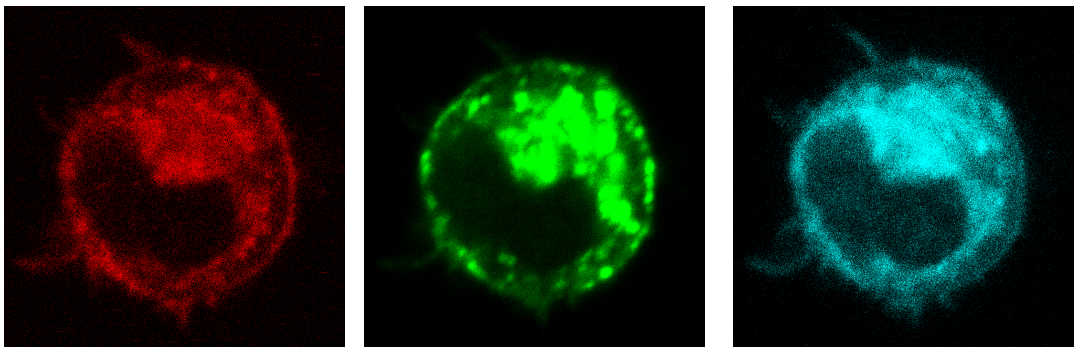

(a) (b) (c)

Figure 4.13: *Three channels of a T-cell taken with confocal microscope from left to right: α-CD59 Alexa Fluor-647 conjugate (a), CT-B with Alexa Fluor-488 conjugate (b), C-Laurdan (c).*

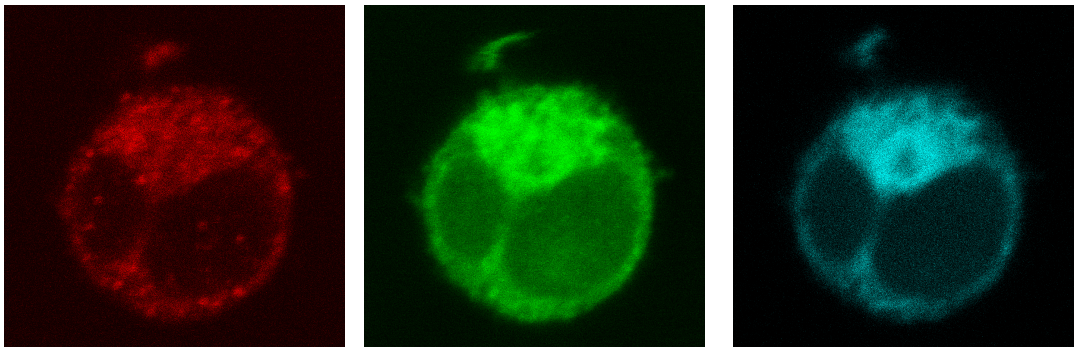

(a) (b) (c)

Figure 4.14: *Three channels of a T-cell taken with confocal microscope from left to right: α-TfR Alexa-647 conjugate (a), CT-B with Alexa Fluor-488 conjugate (b), C-Laurdan (c).*

Figure 4.15 present the Pearson and Spearman rank correlation coefficients between the two species and each species with the membrane, together with the confidence interval for the correlation coefficients at $\alpha = 0.05$ significance level. The difference in correlation coefficient before and after normalization is significant, however the correlation between each species increase after normalization. Studying the correlation between each species and the background, the correlation coefficients after normalization are large and negative. This indicates that instead of removing a dependency between species and background, a dependency is created when weighting the intensity of the two species with the background intensity. These results can be compared with the last simulation presented above, where

a false correlation is created between two species after weighting their intensities with the background.

In order to attempt to reduce the impact of noise on the correlation the GPR interpolation of each channel in figure 4.13 and 4.14 was used to calculate the correlation. The Pearson and Spearman rank correlation coefficients of the normalized GPR interpolated intensities are also presented in figure 4.15. We note that the same behaviour remains for first image (figure 4.13), but not for the second image (figure 4.14). A plausible explanation for this is that a large part of the added dependency originates from the effect or outliers, which is successfully mitigated by the GPR interpolation for the second image, but not in the first.

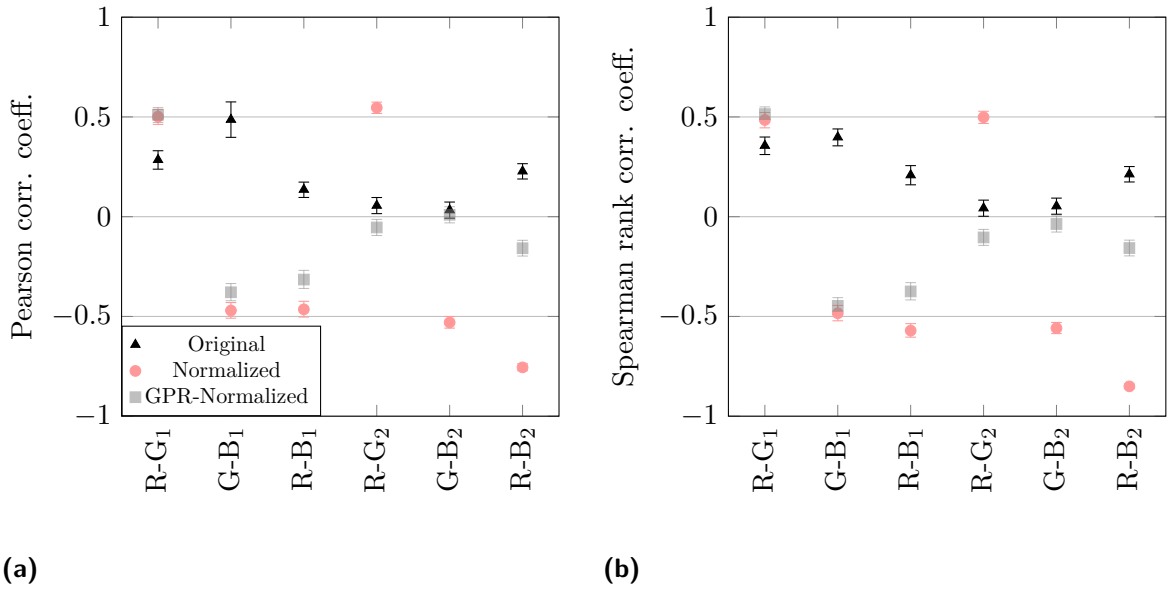

Figure 4.15: *Mean Pearson (a) and Spearman rank (b) correlation coeffiecients and corresponding confidence interval before (black triangles) and after (red circles) normalization, and after normalization with GPR interpolated intensities (gray squares) for the three channels (R,G,B) in figure 4.13 (image 1) and figure 4.14 (image 2).*

As mentioned, the species marked in the cell in figure 4.13 are expected to collocate while the species in figure 4.14 are expected not to collocate. Looking at the correlation coefficients in figure 4.15 the correlation coefficient between the two species in each cell are both relatively low before normalization ($\rho_p = 0.2850$ and $\rho_p = 0.0558$ respectively). This might be an effect of poor signal strength, especially in the red and blue channels, as seen in figure 4.13. It could also be an effect of sample preparation such as unsuccessful patching of CT-B. It is possible that some of the analytical methods presented in section 2 such as RBNCC would yield different results on the correlation calculations. However during imaging, we experienced problems with photobleacing of C-Laurdan, a known drawback of the fluorophore, and two subsequent images of sufficient quality could not be acquired.

5 Conclusion

It has been shown that the plasma membrane of cells is not flat, but can be folded and convoluted. Under this assumption simulations of two species on a series of non-uniform backgrounds were made. The simulated images were normalized by weighting the species' intensities in each pixel by the corresponding pixel intensity of the background. By calculating the Pearson and Spearman correlation coefficients between the two species before and after normalization, we show a significant decrease in correlation coefficient after background normalization (significance level $\alpha = 0.05$).

As expected, the correlation coefficient between the two simulated species before normalization is higher than the corresponding correlation coefficient of two simulated species on a uniform surface. This proved to be true for all proportions of collocation proportion, which is expected to correlate with the correlation coefficient. For large sample sizes ($n = 5000$) before normalization, the correlation coefficient lies between 0.9 and 1 for all collocation proportions. Our results show that after background normalization, the correlation coefficient approach the value of the simulations' collocation, for all collocation proportions between $p = 0$ and $p = 1$. From this we conclude that two species on a non-uniform surface will indeed be falsely correlated, and this false correlation can be successfully mitigated by removing each species dependency on the background.

The dependency between species and background in our simulations is very high, as probability of finding a species in a specific location varies from zero to one, ie. non-existent to absolutely certain. This is not the case in reality, where there will never be zero or infinitely much membrane in any location. Taking this into consideration may yield simulations that are more representative of reality. Similarly, in colocalization experiments the background is also studied by fluorescence microscopy and will be subject to the same PSF distortion as the the species. For a more life-like simulation the background should be passed through the same Gaussian filter as the species before normalization.

We also show that if the species are independent of the background, attempts to normalize will effectively create a dependency between species and background. As seen in the simulations described above, such a fabricated dependency between each species and the background will in turn create a false correlation between the two individual species. This result is also found in the correlation calculations of the experimental images where the correlation coefficient between two species increased after background normalization. Another assumption this method makes is a linear relationship between the intensity of the species and the background, an assumption which may be false. Instead the relationship between species and background may be more complex, in which case other methods of correction must be considered.

The signal of the experimental images were low, especially in the channel containing the signal from the background. It is therefore likely that any variance in signal caused by membrane topography is smaller than that of the noise, making this variance impossible to detect. In order to make a representative evaluation of the normalization method the images acquired must be of sufficient quality, preferably using a membrane marker less prone to photobleaching than C-Laurdan, which would allow for acquisition of subsequent images without loss of signal.

From this project we draw the conclusions that background normalization effectively

removes the dependency between species and background, given that such dependency exists in the first place. If there is no dependency between species and background, background normalization by intensity division will instead result in the creation of one. Because of this, it is important to have knowledge of the biology behind the experiment and only normalize the intensities of the species with respect to the background if a large effect of background topography is expected. Therefor, the first step of a colocalization analysis should be to independently investigate the correlation between each species and the background they live on, in order to determine whether a dependency exists or not.

References

[1] Tony Magee et al. “Lipid rafts: cell surface platforms for T cell signaling”. In: *Biological Research* 35 (2002), pp. 127–131. ISSN: 0716-9760. DOI: 10.4067/s0716-97602002000200003.

[2] Anna M. Lipp et al. “Lck mediates signal transmission from CD59 to the TCR/CD3 pathway in Jurkat T cells”. In: *PLoS ONE* 9 (1 Jan. 2014). ISSN: 19326203. DOI: 10.1371/journal.pone.0085934.

[3] Jelena Dinic, Parham Ashrafzadeh, and Ingela Parmryd. “Actin filaments attachment at the plasma membrane in live cells cause the formation of ordered lipid domains”. In: *Biochimica et Biophysica Acta - Biomembranes* 1828 (3 2013), pp. 1102–1111. ISSN: 00052736. DOI: 10.1016/j.bbamem.2012.12.004.

[4] Jeremy Adler et al. “Plasma membrane topography and interpretation of single-particle tracks”. In: *Nature Methods* 7 (3 2010), pp. 170–171. ISSN: 15487091. DOI: 10.1038/nmeth0310-170.

[5] Geoffrey M. Cooper and Robert E. Hausman. *The Cell: A Molecular Approach.* 7th ed. Sunderland, MA: Sinauer Associates is an imprint of Oxford University Press, 2016, pp. 70–74, 531–444. ISBN: 978-1-60535-290-9.

[6] Peter W Janes, Steven C Ley, and Anthony I Magee. *Aggregation of Lipid Rafts Accompanies Signaling Via the T Cell Antigen Receptor.* 1999, pp. 447–461. DOI: https://doi.org/10.1083/jcb.147.2.447.

[7] Ingela Parmryd et al. “Imaging metabolism of phosphatidylinositol 4,5-bisphosphate in T-cell GM1-enriched domains containing Ras proteins”. In: *Experimental Cell Research* 285 (1 2003), pp. 27–38. ISSN: 00144827. DOI: 10.1016/S0014-4827(02)00048-4.

[8] S Bolte and F. P. Cordelieres. “A guided tour into subcellular colocalization analysis in light microscopy”. In: *Journal of Microscopy* 224 (2006), pp. 213–232.

[9] David J. C. MacKay. *Information theory, inference, and learning algorithms.* Cambridge University Press, 2003. ISBN: 0521642981.

[10] Jeremy Adler and Ingela Parmryd. “Colocalization Analysis in Fluorescence Microscopy”. In: *Cell Imaging Techniques.* Ed. by Douglas J. Taatjes and Jürgen Roth. New York, NY: Humana Press, 2012, pp. 97–109.

[11] Thibault Lagache et al. “Statistical analysis of molecule colocalization in bioimaging”. In: *Cytometry A.* 87.6 (2015), pp. 568–579.

[12] Jean-Christophe Olivo-Marin. “Extraction of spots in biological images using multiscale products”. In: *Pattern Recognition* 35 (2002), pp. 1989–1996. DOI: https://doi.org/10.1016/S0031-3203(01)00127-3.

[13] Thibault Lagache, Vannary Meas-Yedid, and Jean Christophe Olivo-Marin. “A statistical analysis of spatial colocalization using Ripley’s K function”. In: 2013, pp. 896–901. ISBN: 9781467364546. DOI: 10.1109/ISBI.2013.6556620.

[14] B D Ripley. “Modelling Spatial Patterns”. In: *Journal of the Royal Statistical Society: Series B (Methodological)* 39 (2 1977). DOI: https://doi.org/10.1111/j.2517-6161.1977.tb01615.x.

[15] Lei Xu et al. “Resolution, target density and labeling effects in colocalization studies – suppression of false positives by nanoscopy and modified algorithms”. In: *The FEBS Journal* 283.5 (2016), pp. 882–898.

[16] John A. Rice. *Mathematical Statistics and Data Analysis*. Belmont, CA: Brooks/-Cole, 2007, p. 406. ISBN: 978-0-495-11868-8.

[17] J. Adler, S. N. Pagakis, and I. Parmryd. “Replicate-based noise corrected correlation for accurate measurements of colocalization”. In: *Journal of Microscopy* 230 (2008), pp. 121–133.

[18] Jesse S. Aaron, Aaron B. Taylor, and Teng Leong Chew. “Image co-localization - Co-occurrence versus correlation”. In: *Journal of Cell Science* 131 (3 2018). ISSN: 14779137. DOI: 10.1242/JCS.211847.

[19] Erik M. M. Manders, F. Verbeek, and J. A. Aten. “Measurement of co-localization of objects in dual-colour confocal images”. In: *Journal of Microscopy* 169 (1993).

[20] Samuel W. Hasinoff. “Photon, Poisson Noise”. In: *Computer Vision: A Reference Guide*. Ed. by Katsushi Ikeuchi. Boston, MA: Springer US, 2014, pp. 608–610. ISBN: 978-0-387-31439-6. DOI: 10.1007/978-0-387-31439-6_482.

[21] Sylvain V. Costes et al. “Automatic and quantitative measurement of protein-protein colocalization in live cells”. In: *Biophysical Journal* 86 (6 2004), pp. 3993–4003. ISSN: 00063495. DOI: 10.1529/biophysj.103.038422.

[22] Bas van Steensel et al. “Partial colocalization of glucocorticoid and mineralocorticoid receptors in discrete compartments in nuclei of rat hippocampus neurons”. In: *Journal of Cell Science* 109 (1996), pp. 787–792.

[23] Huaizhi Yang, R. Michael E. Parkhouse, and Thomas Wileman. “Monoclonal antibodies that identify the CD3 molecules expressed specifically at the surface of porcine $\gamma\delta$-T cells”. In: *Immunology* 115 (2 June 2005), pp. 189–196. ISSN: 00192805. DOI: 10.1111/j.1365-2567.2005.02137.x.

[24] Charles A. Day and Anne K. Kenworthy. “Functions of cholera toxin B-subunit as a raft cross-linker”. In: *Essays in Biochemistry* 57 (2015), pp. 135–145. ISSN: 00711365. DOI: 10.1042/BSE0570135.

[25] Francisco J. Barrantes. “Chapter Nine - Fluorescence sensors for imaging membrane lipid domains and cholesterol”. In: *New Methods and Sensors for Membrane and Cell Volume Research*. Ed. by Michael A. Model and Irena Levitan. Vol. 88. Current Topics in Membranes. Academic Press, 2021, pp. 257–314. DOI: https://doi.org/10.1016/bs.ctm.2021.09.004. URL: https://www.sciencedirect.com/science/article/pii/S1063582321000132.

[26] Talley J. Lambert. “FPbase: a community-editable fluorescent protein database”. In: *Nature Methods* 16 (2019), pp. 277–278. DOI: https://doi.org/10.1038/s41592-019-0352-8.

[27] bio-techne. *C-Laurdan*. https://www.bio-techne.com/p/fluorescent-probes-dyes/c-laurdan_7273#technical-data-tab-tab. Accessed: 2022-03-15.

[28] Seong Oh Kim et al. “Mechanical properties of paraformaldehyde-treated individual cells investigated by atomic force microscopy and scanning ion conductance microscopy”. In: *Nano Convergence* 4 (1 2017). ISSN: 21965404. DOI: 10.1186/s40580-017-0099-9.

[29] Peter W Janes, Steven C Ley, and Anthony I Magee. “Aggregation of Lipid Rafts Accompanies Signaling Via the T Cell Antigen Receptor”. In: *The Journal of Cell Biology* 147 (2 1999), pp. 447–461. DOI: https://doi.org/10.1083/jcb.147.2.447.

[30] Mats Rudemo. *STATISTICS OF IMAGING*. Book Manuscript. 2020.

[31] “Log Gaussian Cox Processes”. In: *Scandinavian Journal of Statistics* 25.3 (1998), pp. 451–482. ISSN: 03036898, 14679469.

A Appendix

A.1 Protocols

This appendix contain the protocols used during the experimental work and are presented as basis for replicability.

A.1.1 TESPA coating of coverslips

1. Wash coverslips in 10%HCl/70%EtOH.
2. Wash coverslips in H_2O.
3. Wash coverslips in acetone.
4. Add coverslips individually to 1mL TESPA/50 mL acetone and leave for at least five minutes. Flip the tube occasionally.
5. Wash coverslips twice with acetone.
6. Wash coverslips in H_2O.
7. Leave to dry on paper.
8. Store protected from dust.

A.1.2 Cell staining with C-laurdan, cholera toxin and antibodies

- **Prepare cells**
  1. Wash and pellet cells.
  2. Resuspend cells in PBS to a concentration of $1.25 \cdot 10^6$ cells/mL.
  3. Place 200 µL cellsuspension at the centre of TESPA covered coverslips. Leave on ice for 30-45 min.
- **Cholera Toxin and membrane staining**
  1. Add 50 µL CT-B-fluorophore conjugate in 0.1% BSA/PBS.
  2. Incubate on ice 30min.
  3. Remove fluid.
  4. Add 50 µL anti-CT-B in 0.1% BSA/PBS.
  5. Incubate on ice 30min.
  6. Remove fluid.
  7. Add 200 µL C-Laurdan.
  8. Incubate at 37 °C 20 min.
  9. Remove fluid.
  10. Fix in 100 µL 4% PFA/PBS at 37°C 15min.
  11. Wash 3 times with PBS.
- **Antibody staining**
  1. Block in 200 µL 2% BSA/PBS on ice for at least 20min.
  2. Add primary antibody 50 µL in 2% BSA/PBS.
  3. Incubate at room temperature 30 min.
  4. Wash 3 times with PBS.
  5. Add primary antibody 50 µL in 2% BSA/PBS.
  6. Incubate at room temperature 15 min.

7. Wash 3 times with PBS.
8. Add 200 µL C-Laurdan.
9. Incubate at room temperature 20 min.
10. Wash 3 times with PBS.

- **Mounting**
  1. Remove excess fluid.
  2. Mount with AF1.
  3. Seal with nailpolish.